JACS
JOURNAL OF THE AMERICAN CHEMICAL SOCIETY

Subscriber access provided by American Chemical Society

Article

Transparent Conducting Oxides: Texture and Microstructure Effects on Charge Carrier Mobility in MOCVD-Derived CdO Thin Films Grown with A Thermally Stable, Low-Melting Precursor

Andrew W. Metz, John R. Ireland, Jian-Guo Zheng, Ricardo P. S. M. Lobo, Yu Yang, Jun Ni, Charlotte L. Stern, Vinayak P. Dravid, Nicole Bontemps, Carl R. Kannewurf, Kenneth R. Poeppelmeier, and Tobin J. Marks

J. Am. Chem. Soc., **2004**, 126 (27), 8477-8492• DOI: 10.1021/ja039232z • Publication Date (Web): 19 June 2004

Downloaded from http://pubs.acs.org on March 31, 2009

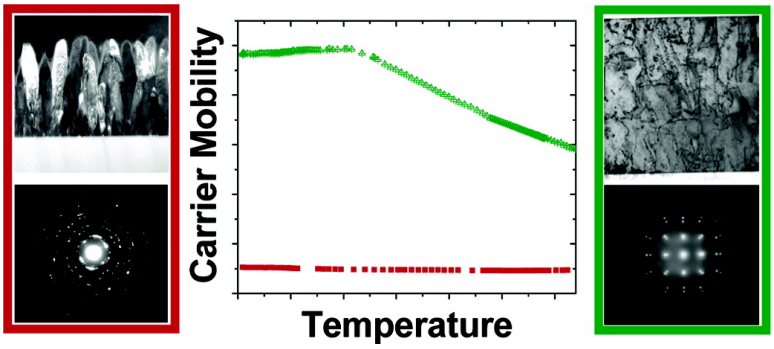

More About This Article

Additional resources and features associated with this article are available within the HTML version:

- Supporting Information
- Links to the 5 articles that cite this article, as of the time of this article download
- Access to high resolution figures
- Links to articles and content related to this article
- Copyright permission to reproduce figures and/or text from this article

View the Full Text HTML

ACS Publications
High quality. High impact.

Journal of the American Chemical Society is published by the American Chemical Society. 1155 Sixteenth Street N.W., Washington, DC 20036

J|A|C|S
ARTICLES
Published on Web 06/19/2004

Transparent Conducting Oxides: Texture and Microstructure Effects on Charge Carrier Mobility in MOCVD-Derived CdO Thin Films Grown with A Thermally Stable, Low-Melting Precursor

Andrew W. Metz, John R. Ireland,† Jian-Guo Zheng,‡ Ricardo P. S. M. Lobo,§ Yu Yang, Jun Ni, Charlotte L. Stern, Vinayak P. Dravid,‡ Nicole Bontemps,§ Carl R. Kannewurf,† Kenneth R. Poeppelmeier, and Tobin J. Marks*

Contribution from the Department of Chemistry, Department of Electrical and Computer Engineering, Department of Materials Science and Engineering, and the Materials Research Center, Northwestern University, Evanston, Illinois 60208-3113, and Laboratoire de Physique du Solide, Ecole Supérieure de Physique et Chimie Industrielles de la Ville de Paris, CNRS UPR 5, 75321 Paris Cedex 5, France

Received October 25, 2003; E-mail: t-marks@northwestern.edu

Abstract: A series of low-melting, thermally stable cadmium metal−organic chemical vapor deposition (MOCVD) precursors have been synthesized, structurally and spectroscopically characterized, and implemented in growth of highly conductive and transparent CdO thin films. One member of the series, bis(1,1,1,5,5,5-hexafluoro-2,4-pentanedionato)(*N,N*-diethyl-*N′,N′*-dimethyl-ethylenediamine)cadmium(II), *Cd(hfa)$_2$(N,N-DE-N′,N′-DMEDA),* represents a particularly significant improvement over previously available Cd precursors, owing to the low melting point and robust thermal stability. High-quality CdO films were grown by MOCVD on glass and single-crystal MgO(100) between 300 and 412 °C. Film growth parameters and substrate surface have large effects on microstructure and electron carrier transport properties. Enhanced mobilities observed for highly biaxially textured films grown on MgO(100) vs glass are attributed, on the basis of DC charge transport and microstructure analysis, to a reduction in neutral impurity scattering and/or to a more densely packed grain microstructure. Although single-grained films grown on MgO(100) exhibit greater mobilities than analogues with discrete ∼100 nm grains and similar texture, this effect is attributed, on the basis of charge transport and Hall effect measurements as well as optical reflectivity analysis, to differences in carrier concentration rather than to reduced grain boundary scattering. Unprecedented conductivities and mobilities as high as 11,000 S/cm and 307 cm^2/V·s, respectively, are obtained for epitaxial single-grained films (X-ray diffraction parameters: fwhm$_\omega$ = 0.30°, fwhm$_\phi$ = 0.27°) grown in situ on MgO(100) at a relatively low temperature (400 °C).

Introduction

Cadmium-containing thin films are used in a wide variety of applications such as transparent conducting oxides[1−3] (TCOs) and photovoltaic (PV) active layers.[4] The widespread use of TCOs as transparent electrodes in many advanced technology applications has led to the intense investigation of their chemical/physical/optoelectronic nature; although TCOs are used on the scale of billions of dollars per year, their properties are still poorly understood. Importantly, improved TCO materials could have an enormous impact on next-generation flat-panel displays and solar energy systems, and progress in this field will require a dedicated, multidisciplinary effort. For general discussions of TCO science and technology issues, the reader is referred to a number of excellent recent reviews.[2,5]

To realize future optoelectronic device applications, next-generation TCO materials must be far more conductive, while preserving or improving transparency and maintaining an appreciable band gap (for optical transparency). The most attractive way to achieve these ends is by increasing carrier mobility since this has no detrimental effects on optical properties. An optimum carrier concentration that maximizes

† Department of Electrical and Computer Engineering, Northwestern University.
‡ Materials Research Center, Northwestern University.
§ Laboratoire de Physique du Solide, Ecole Supérieure de Physique et Chimie Industrielles de la Ville de Paris.

(1) (a) Mason, T. O.; Gonzalez, G. B.; Kammler, D. R.; Mansourian-Hadavi, N.; Ingram, B. J. *Thin Solid Films* **2002**, *411*, 106−114. (b) Kammler, D. R.; Mason, T. O.; Young, D. L.; Coutts, T. J. *J. Appl. Phys.* **2001**, *90*, 3263−3268. (c) Coutts, T. J.; Young, D. L.; Li, X. *Mater. Res. Soc. Symp. Proc.* **2000**, *623*, 199−209. (d) Chopra, K. L.; Major, S. *Proc. - Electrochem. Soc.* **1983**, *83−11*, 346−358.
(2) (a) Freeman, A. J.; Poeppelmeier, K. R.; Mason, T. O.; Chang, R. P. H.; Marks, T. J. *MRS Bull.* **2000**, *25*, 45−51. (b) Coutts, T. J.; Young, D. L.; Li, X. *MRS Bull.* **2000**, *25*, 58−65. (c) Ginley, D. S.; Bright, C. *MRS Bull.* **2000**, *25*, 15−21.
(3) Coutts, T. J.; Young, D. L.; Li, X.; Mulligan, W. P.; Wu, X. *J. Vac. Sci. Technol., A* **2000**, *18*, 2646−2660.
(4) (a) Mathew, X.; Thompson, G. W.; Singh, V. P.; McClure, J. C.; Velumani, S.; Mathews, N. R.; Sebastian, P. J. *Sol. Energy Mater.* **2003**, *76*, 293−303. (b) Marfaing, Y. *J. Phys. IV* **2002**, *12*, 145−154. (c) Martel, A., Caballero-Briones, F., Oliva, A. I., et al. *Phys. Status Solidi B* **2000**, *220*, 261−267. (d) Bonnet, D.; Meyers, P. *J. Mater. Res.* **1998**, *13*, 2740−2753.

the band gap via the carrier concentration-sensitive Moss−Burstein shift,[6] yet maintains a plasma edge removed from the visible region, is desired and in principle achievable via aliovalent doping and/or careful control of the film growth process parameters.[7] This reasoning has motivated recent advances that achieved exceptional carrier mobilities in CdO films.[3,7−14] Although CdO has a relatively low intrinsic band gap of 2.28 eV,[15] its low effective carrier mass[7] allows increasing the band gap of heavily doped samples to as high as 3.35 eV[16] and gives rise to mobilities as high as 607 $cm^2/V\cdot s$ in epitaxial, Sn-doped CdO films.[14] Such a mobility is roughly 20× that of commercial tin-doped indium oxide (ITO).

Carrier scattering mechanisms and hypothesized limits to TCO film mobility have been the subject of extensive discussion.[17−21] Mobile carriers in TCOs arise from lattice defects created through nonstoichiometry (oxygen vacancies or cation interstitials) or aliovalent doping (e.g., Sn^{4+} on an In^{3+} site). These point defects are generally ionized and scatter carriers strongly. In other cases, these defects can be compensated (by cation vacancies or associated oxygen clusters), resulting in neutral defects which also can scatter carriers. Individual grains in a polycrystalline film are connected by transitional regions where lattice defects can cause charge accumulation and thus a potential barrier that impedes charge transport across the grain boundary interface. While it is generally accepted that ionized impurity scattering (IIS) is the dominant scattering mechanism in TCOs, the roles of neutral impurity scattering (NIS) and grain boundary scattering (GBS) are poorly understood. Dismissed as unimportant in some analyses,[17−19,21,22] examples can also be found where NIS[23−25] and GBS[14,20,26,27] are reported to have pronounced effects on carrier mobilities. Given the large mobility and simple face-centered cubic crystal structure, CdO is an ideally suited model thin-film material for closer examination of these effects.

Metal−organic chemical vapor deposition (MOCVD) is used in many large-volume thin-film manufacturing processes[28] and is particularly attractive for TCO film growth, owing to the conformal, large-area deposition that can be achieved in a relatively simple apparatus, and at closer-to-ambient conditions than possible with many physical vapor deposition techniques. However, the need for highly volatile, easy to handle, and thermally stable precursors is a prerequisite for efficient growth by all MOCVD processes. Our continuing interest in the growth of high-mobility, high-transparency CdO-based TCOs of precise composition has necessitated development of more effective metal−organic Cd precursors than are currently available. Until recently, there have been few alternatives to highly toxic[29] and pyrophoric[30] dimethylcadmium. Our group recently reported the first cadmium coordination complex to be successfully utilized as an efficient CdO MOCVD precursor,[9,31] $Cd(hfa)_2(TMEDA)$.

$Cd(hfa)_2(TMEDA)$

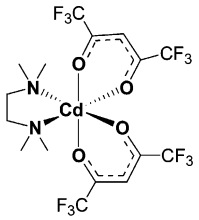

Its many attractive characteristics include a straightforward one-step aqueous synthesis under ambient conditions from commercially available starting materials, excellent volatility, as well as excellent air and thermal stability. There remains, however, a need for complexes that are liquids at growth reactor-operating temperatures, yet are volatile and thermally stable. Solid source precursors, while easy to handle, are prone to sintering, which progressively lowers the surface area (for this type of precursor, deposition is typically diffusion-limited)[32] and gives rise to time-

(5) (a) Granqvist, C. G.; Hultaker, A. *Thin Solid Films* **2002**, *411*, 1−5. (b) Hosono, H.; Ohta, H.; Orita, M.; Ueda, K.; Hirano, M. *Vacuum* **2002**, *66*, 419−425. (c) Perkins, J. D.; del Cueto, J. A.; Alleman, J. L.; Warmsingh, C.; Keyes, B. M.; Gedvilas, L. M.; Parilla, P. A.; To, B.; Readey, D. W.; Ginley, D. S. *Thin Solid Films* **2002**, *411*, 152−160. (d) Ginley, D.; Coutts, T.; Perkins, J.; Young, D.; Li, X.; Parilla, P.; Stauber, R.; Readey, D.; Duncan, C. *Mater. Res. Soc. Symp. Proc.* **2001**, *668*, H2.7/1−H2.7/15. (e) Kawazoe, H.; Yanagi, H.; Ueda, K.; Hosono, H. *MRS Bull.* **2000**, *25*, 28−36. (f) Lewis, B. G.; Paine, D. C. *MRS Bull.* **2000**, *25*, 22−27. (g) Minami, T. *MRS Bull.* **2000**, *25*, 38−44. (h) Gordon, R. G. *MRS Bull.* **2000**, *25*, 52−57. (i) Coutts, T. J.; Mason, T. O.; Perkins, J. D.; Ginley, D. S. *Proc. - Electrochem. Soc.* **1999**, *99−11*, 274−288. (j) Gordon, R. G. *Mater. Res. Soc. Symp. Proc.* **1996**, *426*, 419−429. (k) Dawar, A. L.; Joshi, J. C. *J. Mater. Sci.* **1984**, *19*, 1−23. (l) Jarzebski, Z. M. *Phys. Status Solidi A* **1982**, *71*, 13−41.
(6) Hamberg, I.; Granqvist, C. G. *J. Appl. Phys.* **1986**, *60*, R123−R159.
(7) Wang, A.; Babcock, J. R.; Edleman, N. L.; Metz, A. W.; Lane, M. A.; Asahi, R.; Dravid, V. P.; Kannewurf, C. R.; Freeman, A. J.; Marks, T. J. *Proc. Natl. Acad. Sci. U.S.A.* **2001**, *98*, 7113−7116.
(8) Barnes, T. M.; Li, X.; DeHart, C.; Moutinho, H.; Asher, S.; Yan, Y.; Gessert, T. A. *Mater. Res. Soc. Symp. Proc.* **2001**, *666*, F1.8/1−F1.8/6.
(9) Babcock, J. R.; Wang, A.; Metz, A. W.; Edleman, N. L.; Metz, M. V.; Lane, M. A.; Kannewurf, C. R.; Marks, T. J. *Chem. Vap. Deposition* **2001**, *7*, 239−242.
(10) Asahi, R.; Wang, A.; Babcock, J. R.; Edleman, N. L.; Metz, A. W.; Lane, M. A.; Dravid, V. P.; Kannewurf, C. R.; Freeman, A. J.; Marks, T. J. *Thin Solid Films* **2002**, *411*, 101−105.
(11) Asahi, R.; Babcock, J. R.; Edleman, N. L.; Kammler, D. R.; Ko, D.; Lane, M. A.; Metz, A. W.; Wang, A.; Yan, M.; Chang, R. P. H.; Dravid, V.; Freeman, A. J.; Kannewurf, C. R.; Marks, T. J.; Mason, T. O.; Poeppelmeier, K. R. *Proc. - Electrochem. Soc.* **2001**, *2001−10*, 333−348.
(12) Li, X.; Barnes, T. M.; DeHart, C.; King, D.; Asher, S.; Young, M.; Gessert, T. A.; Coutts, T. J. *Mater. Res. Soc. Symp. Proc.* **2001**, *666*, F3.18.11.
(13) (a) Li, X.; Yan, Y.; Mason, A.; Gessert, T. A.; Coutts, T. J. *Electrochem. Solid-State Lett.* **2001**, *4*, C66−C68. (b) Li, X.; Young, D. L.; Moutinho, H.; Yan, Y.; Narayanswamy, C.; Gessert, T. A.; Coutts, T. J. *Electrochem. Solid-State Lett.* **2001**, *4*, C43−C46.
(14) Yan, M.; Lane, M.; Kannewurf, C. R.; Chang, R. P. H. *Appl. Phys. Lett.* **2001**, *78*, 2342−2344.
(15) Ueda, N.; Maeda, H.; Hosono, H.; Kawazoe, H. *J. Appl. Phys.* **1998**, *84*, 6174−6177.
(16) Zhao, Z.; Morel, D. L.; Ferekides, C. S. *Thin Solid Films* **2002**, *413*, 203-211.
(17) Chen, M.; Pei, Z. L.; Wang, X.; Yu, Y. H.; Liu, X. H.; Sun, C.; Wen, L. S. *J. Phys. D: Appl. Phys.* **2000**, *33*, 2538−2548.
(18) Zhang, D. H.; Ma, H. L. *Appl. Phys. A* **1996**, *A62*, 487−492.
(19) Chen, M.; Pei, Z.; Wang, X.; Sun, C.; Wen, L. *Mater. Res. Soc. Symp. Proc.* **2001**, *666*, F2.3/1−F2.3/6.
(20) Minami, T.; Suzuki, S.; Miyata, T. *Mater. Res. Soc. Symp. Proc.* **2001**, *666*, F1.3/1−F1.3/7.
(21) Gilmore, A. S.; Al-Kaoud, A.; Kaydanov, V.; Ohno, T. R. *Mater. Res. Soc. Symp. Proc.* **2001**, *666*, F3.10/11−F13.10/16.
(22) Kamei, M.; Yagami, T.; Takaki, S.; Shigesato, Y. *Appl. Phys. Lett.* **1994**, *64*, 2712−2714.
(23) Taga, N.; Odaka, H.; Shigesato, Y.; Yasui, I.; Kamei, M.; Haynes, T. E. *J. Appl. Phys.* **1996**, *80*, 978−984.
(24) Tahar, R. B. H.; Tahar, N. B. H. *J. Appl. Phys.* **2002**, *92*, 4498−4501.
(25) Young, D. L.; Coutts, T. J.; Kaydanov, V. I.; Gilmore, A. S.; Mulligan, W. P. *J. Vac. Sci. Technol., A* **2000**, *18*, 2978−2985.
(26) Kim, H.; Horwitz, J. S.; Qadri, S. B.; Chrisey, D. B. *Thin Solid Films* **2002**, *420−421*, 107−111.
(27) Shanthi, E.; Banerjee, A.; Dutta, V.; Chopra, K. L. *J. Appl. Phys.* **1982**, *53*, 1615−1621.
(28) (a) Choy, K. L. *Prog. Mater Sci.* **2003**, *48*, 57−170. (b) Waser, R.; Schneller, T.; Hoffmann-Eifert, S.; Ehrhart, P. *Integr. Ferroelectr.* **2001**, *36*, 3−20. (c) Just, O.; Rees, W. S., Jr. *Adv. Mater. Opt. Electron.* **2000**, *10*, 213−221. (d) Winter, C. H. *Aldrichimica Acta* **2000**, *33*, 3−12. (e) Gordon, R. *J. Non-Cryst. Solids* **1997**, *218*, 81−91. (f) Schulz, D. L.; Marks, T. J. *CVD Nonmetals* **1996**, 37−150.
(29) Spiridonova, E. Y. *Gig. Tr. Prof. Zabol.* **1991**, 14−17.
(30) Zorin, A. D.; Emel'yanova, O. A.; Zanozina, V. F.; Markova, M. L.; Karataev, Y. N.; Stepanova, L. V.; Feshchenko, I. A. *Zh. Prikl. Spektrosk.* **1989**, *51*, 903−906.
(31) Babcock, J. R.; Wang, A.; Edleman, N. L.; Benson, D. D.; Metz, A. W.; Metz, M. V.; Marks, T. J. *Mater. Res. Soc. Symp. Proc.* **2000**, *623*, 317−328.
(32) Hinds, B. J.; McNeely, R. J.; Studebaker, D. B.; Marks, T. J.; Hogan, T. P.; Schindler, J. L.; Kannewurf, C. R.; Zhang, X. F.; Miller, D. J. *J. Mater. Res.* **1997**, *12*, 1214−1236.

dependent volatilization rates. In contrast, liquid precursors have a constant surface area that provides stable precursor delivery.[33−35] A $Cd(hfa)_2$(TMEDA) analogue with a lower melting point would be highly desirable if it were a liquid at standard MOCVD growth reactor-operating temperatures, while maintaining robust thermal properties. It is well-established that appropriate substitutions at the ligand periphery can be used to tailor melting points in related types of Group II precursors without deleterious impact on volatility or thermal stability.[35,36] Complementary approaches to low-melting cadmium precursors have very recently been reported.[37,38]

In this contribution, we discuss the design, synthesis, and structural characterization of a series of low-melting and thermally stable cadmium MOCVD precursors. We then demonstrate their efficacious properties with thermogravimetric analysis and growth of high-quality CdO films. Detailed comparison of CdO film microstructure and optical and charge transport properties for specimens grown in parallel on both amorphous and single-crystal substrates provides evidence that epitaxy can greatly enhance charge carrier mobility in TCO thin films. This mechanistic information provides insight into strategies for producing very high-mobility TCOs for next-generation optoelectronic applications. Beyond TCO applications, this work provides guidance for tailoring the optoelectronic properties of degenerate semiconductors in general and describes the chemical synthesis of precursors which can be used for the efficient study of a broad range of cadmium-based materials prepared via MOCVD techniques.

Experimental Section

Reagents. All reagents were used as received. $Cd(NO_3)_2{\cdot}4H_2O$ (99.999% metal purity) was obtained from Aldrich, 1,1,1,5,5,5 hexafluoro-2,2-pentanedione from Oakwood Chemicals, and the diamines from Aldrich, Lancaster, or Pfaltz and Bauer. Deuterated NMR solvents were obtained from Cambridge Isotope Laboratories, Inc.

Physical Measurements. Standard NMR spectra were obtained on a Varian Inova 500 MHz spectrometer in benzene-d_6. Variable-temperature (VT) NMR spectra were obtained in toluene-d_8. Chemical shifts are referenced to the residual protonated solvent resonance. Elemental analyses were preformed by Midwest Microlabs, Inc. (Indianapolis, IN). Melting points were measured in sealed glass capillaries with a MelTemp melting point apparatus. Thermogravimetric analysis was carried out on a TA Instruments SDT 2960 simultaneous DTA−TGA instrument. All TGA data were collected at a pressure of 5.00 ± 0.05 Torr of N_2. Weight loss curves were obtained at a ramp rate of 1.5°C/min.

General Synthetic Procedure for Cd MOCVD Precursors. A single-neck, 2-L round-bottom flask is charged with $Cd(NO_3)_2{\cdot}4H_2O$ (99.999% metals purity; 139 mmol), 400 mL of deionized H_2O, and diamine (139 mmol, 1.0 equiv). Next, a 450 mL solution of 1,1,1,5,5,5-hexafluoro-2,4-pentanedione (278 mmol, 2.0 equiv) and NaOH (278 mmol, 2.0 equiv) in methanol/water (10:1) is slowly added under constant stirring. A colorless solid precipitates, and the resultant mixture is stirred for an additional 60 min. The solid is then collected by filtration using a glass frit, washed with H_2O, and dried over P_4O_{10} in a vacuum desiccator. The crude product is then vacuum sublimed (80 °C/1 × 10^{-4} Torr). A typical purified product yield of >70% is obtained.

Bis(1,1,1,5,5,5-hexafluoro-2,4-pentanedionato)(*N,N*-diethylethylenediamine)cadmium(II), $Cd(hfa)_2$(*N,N*-DEEDA) (1). *Characterization:* mp 119−121 °C; ^{1}H NMR (δ, C_6D_6): 0.66 [t, 6H, C*H*$_3$], 0.90 [s, 2H, NH], 1.68 [s, 2H, Et_2NCH_2], 1.40 [s, 2H, H_2NCH_2], 2.12 [s, 2H, N(C*H*H′CH$_3$)$_2$], 2.55 [s, 2H, N(CH*H*′CH$_3$)$_2$], 6.21 [s, 2H, (CO)-C*H*(CO)]; ^{13}C NMR (δ, C_6D_6): 8.23 [*C*H$_3$], 36.39 [N*C*H$_2$CH$_2$N], 46.08 [N*C*H$_2$CH$_3$], 54.11 [NCH$_2$*C*H$_2$N], 88.89[(CO)*C*H(CO)], 118.25 [q, J = 287.2 Hz, *C*F$_3$], 179.39 [q, J = 33.3 Hz, *C*O]; ^{19}F NMR (δ, C_6D_6): −77.33 [s, 6 F, CF$_3$]. Anal. Calcd for $C_{16}H_{18}F_{12}N_2O_4Cd$: C, 29.90; H, 2.82; N, 4.36. Found: C, 29.80; H, 2.77; N, 4.32.

Bis(1,1,1,5,5,5-hexafluoro-2,4-pentanedionato)(*N,N′*-diethylethylenediamine)cadmium(II), $Cd(hfa)_2$(*N,N′*-DEEDA)(2). *Characterization:* mp 54−56 °C; ^{1}H NMR (δ, C_7D_8, T = 80 °C): 0.86 [t, 6H, C*H*$_3$], 1.22 [s, 2H, N*H*$_2$] 2.05 [s, 4H, NC*H*$_2$CH$_2$N], 2.34 [s, 4H, NC*H*$_2$-CH$_3$], 6.13 [s, 2H, (CO)C*H*(CO)]; ^{13}C NMR (δ, C_7D_8, T = 80 °C): 13.69 [*C*H$_3$], 45.01 [N*C*H$_2$CH$_3$], 47.67[N*C*H$_2$CH$_2$N], 89.09[(CO)*C*H-(CO)], 118.48 [q, J = 287.4 Hz, *C*F$_3$], 179.78 [q, J = 33.3 Hz, *C*O]; ^{19}F NMR (δ, C_6D_6): −77.34. Anal. Calcd for $C_{16}H_{18}F_{12}N_2O_4Cd$: C, 29.90; H, 2.82; N, 4.36. Found: C, 30.23; H, 2.95; N, 4.43.

Bis(1,1,1,5,5,5-hexafluoro-2,4-pentanedionato)(*N,N*-diethyl-*N′,N′*-dimethylethylenediamine)cadmium(II), $Cd(hfa)_2$(*N,N*-DE-*N′,N′*-DMEDA) (3). *Characterization:* mp 64−66 °C; ^{1}H NMR (δ, C_6D_6): 0.68 [t, 6H, N(CH$_2$C*H*$_3$)$_2$], 1.79 [m, 2H, NC*H*$_2$CH$_2$N], 1.90 [m, 2H, NC*H*$_2$CH$_2$N], 1.93 [s, 6H, N(C*H*$_3$)$_2$], 2.21[m, 2H, (N(C*H*H′CH3)$_2$)], 2.62 [m, 2H (N(CH*H*′CH3)$_2$)], 6.19 [s, 2H, (CO)C*H*(CO)]; ^{13}C NMR (δ, C_6D_6): 8.22 [N(CH$_2$*C*H$_3$)$_2$], 46.41 [N(*C*H$_3$)$_2$], 46.48 [N*C*H$_2$CH$_3$], 51.16[N*C*H$_2$CH$_2$N], 55.60 [N*C*H$_2$CH$_2$N], 89.00 [(CO)*C*H(CO)], 118.22 [q, J = 287.2 Hz, *C*F$_3$], 179.58 [q, J = 33.3 Hz, *C*O]; ^{19}F NMR (δ, C_6D_6): −77.42 [CF$_3$]. Anal. Calcd for $C_{18}H_{22}F_{12}N_2O_4Cd$: C, 32.23; H, 3.30; N, 4.17. Found: C, 32.34; H, 3.19; N, 4.07.

Bis(1,1,1,5,5,5-hexafluoro-2,4-pentanedionato)(*N,N′*-diethyl-*N,N′*-dimethylethylenediamine)cadmium(II), $Cd(hfa)_2$(*N,N′*-DE-*N,N′*-DMEDA) (4). *Characterization:* mp 79−81 °C; ^{1}H NMR (δ, C_6D_6): 0.72 [t, 6H, N(CH$_2$C*H*$_3$)$_2$], 0.84 [t, 6H, N(CH$_2$C*H*$_3$)$_2$], 1.49 [d, 2H, NC*H*$_2$CH$_2$N], 1.69 [s, 6H, (NC*H*$_3$)], 1.80 [m, 2H, (NC*H*H′CH3)], 1.88 [s, 6H, (NC*H*$_3$)], 1.96 [m, 2H N(C*H*H′CH3)$_2$)], 2.00 [d, 2H, NC*H*$_2$CH$_2$N], 2.50 [m, 2H, (NCH*H*′CH3)], 2.72 [m, 2H, (NCH-*H*′CH3)], 6.21 [s, 1H, (CO)C*H*(CO)], 6.24 [s, 1H, (CO)C*H*(CO)], ^{13}C NMR (δ, C_6D_6): 9.68 [NCH$_2$*C*H$_3$], 10.17 [NCH$_2$*C*H$_3$], 41.03 [N*C*H$_3$], 42.25 [N*C*H$_3$], 52.64 [N*C*H$_2$CH$_3$], 54.14 [N*C*H$_2$CH$_3$], 54.65 [N*C*H$_2$CH$_2$N], 89.90 [(CO)*C*H(CO)], 118.18 [q, J = 287.4 Hz, *C*F$_3$], 179.55 [q, J = 33.4 Hz, *C*O]; ^{19}F NMR (δ, C_6D_6): −77.49 [CF$_3$], −77.46[CF$_3$]. Anal. Calcd for $C_{18}H_{22}F_{12}N_2O_4Cd$: C, 32.23; H, 3.30; N, 4.17. Found: C, 32.21; H, 3.19; N, 4.07.

Single-Crystal X-ray Diffraction Studies. X-ray data were collected for single crystals of $Cd(hfa)_2$(*N,N*-DEEDA) (**1**) and $Cd(hfa)_2$(*N,N′*-DE-*N,N′*-DMEDA) (**4**) [mounted on glass fibers with Paratone-N (Exxon)] on a SMART-1000 CCD area detector instrument at 153(2) K with graphite monochromated Mo Kα radiation. Colorless platelike crystals of **1** and **4** were grown by the slow evaporation of pentane solutions and had approximate dimensions 0.68 mm × 0.40 mm × 0.17 mm and 0.10 mm × 0.28 mm × 0.30 mm, respectively. A Gaussian face-indexed absorption correction was applied, and data were corrected for Lorentz and polarization effects. The structures were solved by direct methods and expanded using Fourier techniques. All non-hydrogen atoms were refined anisotropically except for disordered fluorine atoms, which were refined with a group isotropic thermal parameter. On the basis of systematic absences and successful solution

(33) (a) Yoshida, Y.; Ito, Y.; Hirabayashi, I.; Nagai, H.; Takai, Y. *Appl. Phys. Lett.* **1996**, *69*, 845−847. (b) Gordon, R. G. *Proc. - Electrochem. Soc.* **2000**, *2000−13*, 248−259.
(34) Edleman, N. L.; Wang, A.; Belot, J. A.; Metz, A. W.; Babcock, J. R.; Kawaoka, A. M.; Ni, J.; Metz, M. V.; Flaschenriem, C. J.; Stern, C. L.; Liable-Sands, L. M.; Rheingold, A. L.; Markworth, P. R.; Chang, R. P. H.; Chudzik, M. P.; Kannewurf, C. R.; Marks, T. J. *Inorg. Chem.* **2002**, *41*, 5005−5023.
(35) Belot, J. A.; Neumayer, D. A.; Reedy, C. J.; Studebaker, D. B.; Hinds, B. J.; Stern, C. L.; Marks, T. J. *Chem. Mater.* **1997**, *9*, 1638−1648.
(36) Hatanpaeae, T.; Kansikas, J.; Mutikainen, I.; Leskelae, M. *Inorg. Chem.* **2001**, *40*, 788−794.
(37) (a) Gulino, A.; Castelli, F.; Dapporto, P.; Rossi, P.; Fragala, I. *Chem. Mater.* **2002**, *14*, 704−709. (b) Gulino, A.; Dapporto, P.; Rossi, P.; Fragala, I. *Chem. Mater.* **2002**, *14*, 4955−4962.
(38) Gulino, A.; Dapporto, P.; Rossi, P.; Fragala, I. *Chem. Mater.* **2002**, *14*, 1441−1444.

Table 1. Selected Bond Distances (Å) and Angles (deg) for Complexes **1** and **4**

Bond Distances (Å)			Bond Angles (deg)		
	1	**4**		**1**	**4**
Cd(1)−O(1)	2.276(3)	2.289(4)	O(1)−Cd−O(2)	79.34(10)	78.99(14)
Cd(1)−O(2)	2.322(3)	2.290(4)	O(1)−Cd−O(3)	89.93(11)	171.18(14)
Cd(1)−O(3)	2.272(3)	2.290(4)	O(1)−Cd−O(4)	165.02(11)	94.41(14)
Cd(1)−O(4)	2.290(3)	2.270(4)	O(1)−Cd−N(1)	92.87(11)	98.38(16)
Cd(1)−N(1)	2.388(3)	2.339(5)	O(1)−Cd−N(2)	101.25(13)	89.72(17)
Cd(1)−N(2)	2.277(4)	2.337(6)	O(2)−Cd−O(3)	91.13(11)	94.81(14)
			O(2)−Cd−O(4)	90.03(11)	87.94(19)
			O(2)−Cd−N(1)	168.68(11)	90.42(18)
			O(2)−Cd−N(2)	94.28(12)	163.5(2)
			O(3)−Cd−O(4)	79.66(11)	78.88(13)
			O(3)−Cd−N(1)	97.12(12)	87.98(15)
			O(3)−Cd−N(2)	168.30(13)	97.52(18)
			O(4)−Cd−N(1)	99.04(12)	166.56(17)
			O(4)−Cd−N(2)	89.96(13)	105.1(2)
			N(1)−Cd−N(2)	79.07(12)	79.2(2)

Table 2. MOCVD Growth Conditions for CdO Thin Films

O_2 (H_2O sat.) flow rate	300 sccm
carrier gas (Ar) flow rate	30−80 sccm
precursor reservoir temperature	85 °C
working pressure	4.1 Torr
substrate temperatures	300−425 °C
substrate	1737F glass or MgO(100)

and refinement of the structures, the space groups were determined to be *Pbca* and $P2_1/c$ for complexes **1** and **4**, respectively. Important crystallographic information is summarized in Tables 1 and S1 in Supporting Information.

Film Growth and Characterization. CdO film growth was carried out in a previously described horizontal cold-wall reactor,[32] and growth conditions are compiled in Table 2. The glass precursor reservoir containing **3** was maintained at 85 °C with an ultrahigh purity Ar carrier gas flow rate of 40−80 sccm. The precursor stream was mixed with ultrahigh purity O_2 (flowing at 300 sccm through a water bubbler) immediately upstream of the susceptor. A total working pressure of 4.10 ± 0.05 Torr was maintained for all depositions. Corning 1737F glass and polished MgO(100) substrates were obtained from Precision Glass and Optics and MTI Crystal, respectively. All substrates were cleaned with acetone, placed on the susceptor, dried in an oven at 105°C, and immediately placed in the susceptor holder of the MOCVD reactor laminar flow chamber. Substrate temperatures during film growth were varied from 300 to 412 °C with a growth time of 2 h. Film thickness was measured with a Tencor P-10 step profilometer. X-ray diffraction $\theta-2\theta$ scans of CdO films on glass were obtained with a Rigaku DMAX-A diffractometer using Ni-filtered Cu Kα radiation, while $\theta-2\theta$, ω, and ϕ scans of CdO films on MgO single-crystal substrates were obtained on a Scintag XDS 2000 4-circle diffractometer with detector-selected Cu Kα radiation. Film surface microstructure was imaged on a Hitachi S4500 field emission scanning electron microscope equipped with a light element energy-dispersive X-ray spectrometer (EDS). Transmission electron microscopy (TEM) images, and selected area electron diffraction (SAED) patterns were obtained using a Hitachi 8100 microscope operating at 200 keV. Cross-sectional and plan-view samples were prepared by mechanical grinding, dimpling, and ion milling. Optical transmittance spectra were acquired with a Cary 500 UV−vis−IR spectrophotometer and are referenced to spectra of uncoated substrates. Optical reflectance was measured from 100 to 25 000 cm^{-1} on a Bruker IFS66/v Fourier transform spectrometer. Gold (below 10 000 cm^{-1}) and silver (above 8000 cm^{-1}) mirrors were used as 100% reflectivity references. Variable-temperature Hall effect and four-probe conductivity data were collected between 4 and 330 K, using instrumentation described previously.[39] Quantitative SIMS analysis was performed by MATS (UK) Ltd. Two PLD-derived CdO films, one as-deposited and the second implanted with a known amount of F^- (1E15 ions/cm^2 at 60 keV), were used as standards. Analysis was then performed using a 6 keV Cs^+ ion source in a quadrupole SIMS instrument.

Results

MOCVD Precursor Synthesis and Characterization. Complexes **1**−**4** were prepared by the ambient synthetic route of eq 1—a slight modification of our previously reported method[9,31] using commercially available reagents.

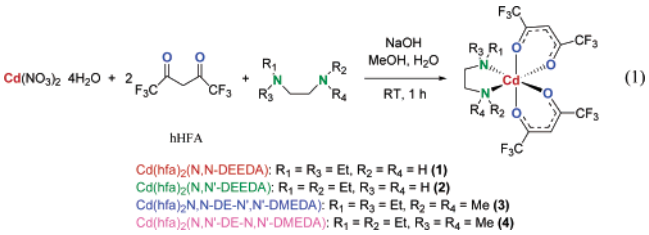

(1)

Complexes **1**−**4** precipitate immediately upon mixing of reagents and, after thorough stirring, are readily isolated by vacuum filtration. Facile purification is accomplished by subsequent vacuum sublimation. All of the new precursors are colorless microcrystalline powders at room temperature and are stable to air, water, and light. The melting points of complexes **1**−**4** are 119−121, 54−56, 64−66, and 79−81 °C, respectively. Note that the melting points are strongly influenced by the diamine architecture.

All new complexes were characterized by ^1H,^{13}C, ^{19}F, ^1H COSY, and $^1H-^{13}C$ HMQC NMR spectroscopy. Spectra for complexes **1** and **3** are consistent with a single species in solution, although the diamine resonances are fairly broad at room temperature and peak multiplicities are not always well-resolved in the ^1H spectra. For complexes **2** and **4,** two structures corresponding to cis and trans dispositions of the *N*-alkyl substituents with respect to the chelate ring plane, are in principle possible. The chelate ring conformations are drawn as observed in the crystal structure and are expected in solution to interconvert rapidly on the NMR time scale.[40]

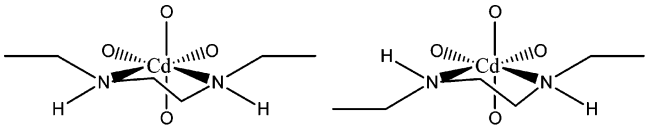

Variable-temperature ^1H NMR spectra of complexes **2** and **4** are shown in Figure 1S, and at low temperatures the spectra are consistent with two isomers in slow-exchange, with approximate 60:40 population ratios. For complex **2**, features within the relatively complicated spectrum acquired at −40 °C broaden and coalesce significantly by 25 °C. At 60 °C, interconversion is rapid on the NMR time scale, and peaks are readily assignable to a single averaged species. Similar behavior is observed for complex **4**, but at much higher temperatures. In each case, the dynamic process must involve stereochemical

(39) Lyding, J. W.; Marcy, H. O.; Marks, T. J.; Kannewurf, C. R. *IEEE Trans. 1nstrum. Meas.* **1988**, *37*, 76−80.
(40) Cotton, F. A.; Wilkinson, G.; Bochmann, M.; Murillo, C. *Advanced Inorganic Chemistry*, 6th ed.; Wiley: New York, 1998; Chapter 1, p 34.

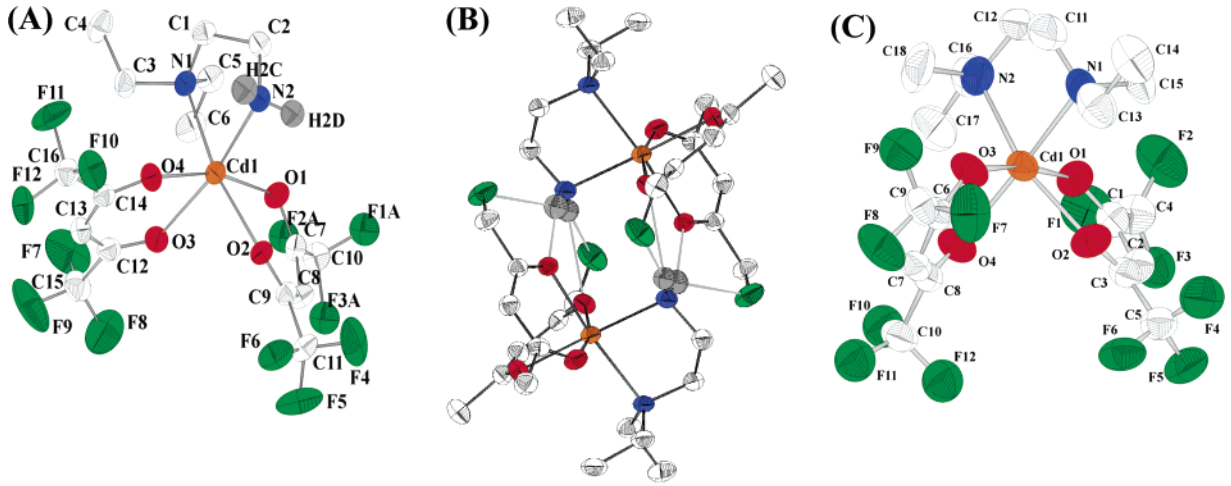

Figure 1. ORTEP drawing (ellipsoids at 50% confidence level) of the: (A) $Cd(hfa)_2$(*N*,*N*-DEEDA) (**1**) molecular structure with atom-labeling scheme. Non-hydrogen-bonded hydrogen atoms and disordered fluorine atoms are omitted for clarity. (B) Dimer structure with non-hydrogen-bonded hydrogen and fluorine atoms omitted for clarity. (C) $Cd(hfa)_2$(*N*,*N*′-DE-*N*,*N*′-DMEDA) (**4**) molecular structure with atom-labeling scheme. Hydrogen atoms and disordered fluorine atoms are omitted for clarity.

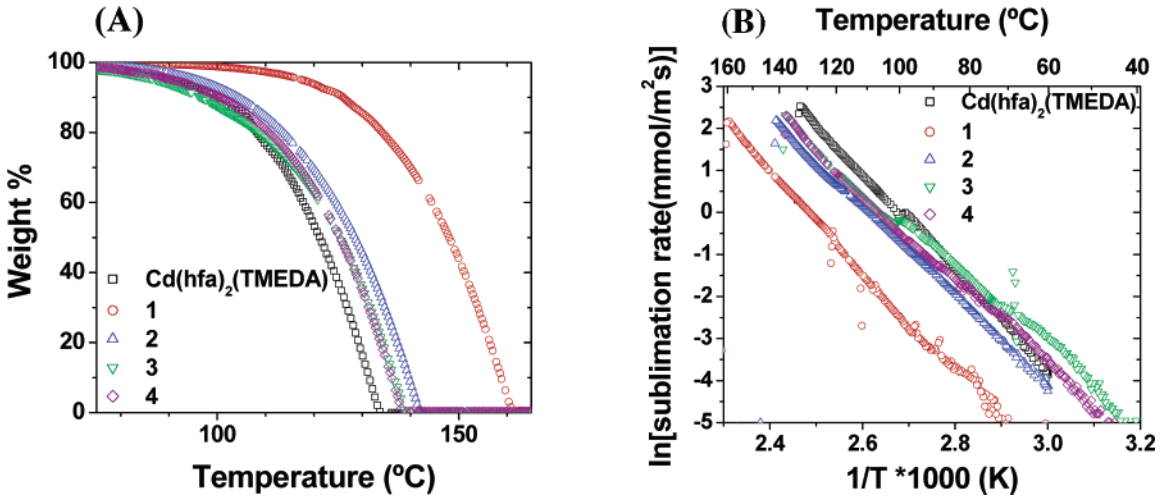

Figure 2. Reduced pressure TGA analysis of the volatility characteristics of $Cd(hfa)_2$(TMEDA) [□], and complexes **1** [red ○], **2** [green △], **3** [blue ▽], and **4** [magenta ◇]. The weight loss (A) and thermal activation (B) data were recorded at a ramp rate of 1.5 °C/min and at 5.00 (±0.05) Torr N_2 pressure.

inversion at one of the coordinated diamine nitrogen atoms. As expected from the coalescence temperatures, estimated activation parameters[41] for this process are much lower for complex **2**. The CH_3 groups of the diamine ethyl substituents are rendered magnetically equivalent at 25 °C ($\Delta G^{\ddagger} = 14.8$ kcal/mol) and 98°C ($\Delta G^{\ddagger} = 18.3$ kcal/mol) for complexes **2** and **4,** respectively. In absence of a labile proton, complex **4** can only undergo inversion preceded by Cd−N bond dissociation.[42] Inversion in complex **2** may be facilitated by base-catalyzed stereoinversion**,** which is well-established for secondary amine metal complexes.[42,43]

Colorless single crystals of **1** and **4** were obtained by slow evaporation of pentane solutions. Both crystal structures (Figure 1) confirm the mononuclearity of the molecular structures, with slightly distorted octahedral coordination at the Cd^{2+} center. Metrical parameters are summarized in Table 1. The Cd−NHEt bond distances in the symmetrical diamine of complex **4** are identical within experimental error (av = 2.338(4) Å). The asymmetric substitution of the diamine in complex **1** leads to significant lengthening of the diethyl substituted Et_2N−Cd bond distance to 2.388(3) Å and a corresponding contraction of the H_2N−Cd bond distance to 2.279(4) Å. The Cd−O bonds trans to the diamine in complex **1** also exhibit bond length distortions: a short Cd−O bond trans to the short Cd−N bond and a long Cd−O bond trans to the long Cd−N bond. Average Cd−N and Cd−O bond distances for complexes **1** and **4** are 2.336(2) Å and 2.287(1) Å, respectively. The present coordination geometries are similar to those observed for $Cd(hfa)_2$-(TMEDA)[9] and $Cd(hfa)_2$(monoglyme)[38] but with slightly longer Cd−ligand contacts.

Reduced pressure thermogravimetric analysis (TGA) data for complexes **1**−**4** are compared to those for $Cd(hfa)_2$(TMEDA) in Figure 2. All precursors exhibit smooth volatilization curves without significant residues (Figure 2A), indicative of a single volatilization process with negligible decomposition. Arrhenius-type thermal activation plots exhibit a linear relationship between

(41) Sandström, J. *Dynamic NMR Spectroscopy*; Academic Press: London; New York, 1982.
(42) Fanizzi, F. P.; Maresca, L.; Natile, G.; Lanfranchi, M.; Manotti-Lanfredi, A. M.; Tiripicchio, A. *Inorg. Chem.* **1988**, *27*, 2422−2431.
(43) (a) Haake, P.; Turley, P. C. *J. Am. Chem. Soc.* **1968**, *90*, 2293−2295. (b) Buckingham, D. A.; Marzilli, L. G.; Sargeson, A. M. *J. Am. Chem. Soc.* **1967**, *89*, 825−830. (c) Buckingham, D. A.; Marzilli, L. G.; Sargeson, A. M. *J. Am. Chem. Soc.* **1968**, *90*, 6028−6032.

Cd(hfa)$_2$(TMEDA)

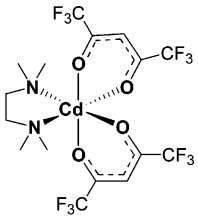

Cd(hfa)$_2$(monglyme)

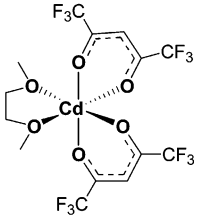

the natural logarithm of the volatilization rate and inverse temperature over standard growth reactor operating temperatures (Figure 2B). All of the present Cd MOCVD precursors have TGA volatilities similar to that of Cd(hfa)$_2$(TMEDA), except complex **1**.

CdO Film Growth and Characterization. Three series of MOCVD-derived CdO films are discussed below. The first two series were grown simultaneously on Corning 1737F glass (softening point: 975 °C) and MgO(100) single-crystal substrates over the temperature range 300−412 °C to study the effects of texture and epitaxy on TCO properties. The third series of films was grown on MgO(100) under the same conditions but at a reduced precursor delivery rate (slower growth) to induce microstructure changes and hence to investigate grain boundary effects on TCO properties.

Glass vs MgO(100). CdO film growth rates were found to be similar for each substrate type, but highly dependent on the substrate temperature during film growth. Film growth rates decrease steadily from 0.82 μm/h to 0.27 μm/h as substrate temperatures increase from 300 to 412 °C. All films are composed of highly crystalline, phase-pure CdO with the cubic rock-salt crystal structure[44] as determined from X-ray diffraction $\theta-2\theta$ scans (Figure 3). Diffraction patterns for CdO films on glass are dominated by a strong (200) reflection. The narrowest rocking curve fwhm of 12° was measured for the (200) reflection of a film grown at 350 °C, indicating that these films have a modest out-of-plane texture (preferred crystallographic orientation normal to the substrate surface). The diffraction data for the CdO films on single-crystal MgO(100) reveal only features from the (200) and (400) reflections of the substrate and film. A high degree of out-of-plane texture is confirmed by the ω-scan[45] fwhm for the (200) reflection which decreases from 1.6° to 0.50° as the deposition temperature is increased from 300 to 400 °C (Figure 4A). In-plane texture (preferred crystallographic orientation in the plane of the substrate surface) was investigated using ϕ scans[46] of the (111) reflections (Figure 4B). The four observed reflections separated by 90° increments and coincident with the (111) of the MgO substrate reflections are consistent with the four-fold cubic symmetry of the CdO fcc lattice and indicate good cube-on-cube alignment. In-plane film texture is also enhanced with increasing deposition temperature as seen from the corresponding narrowing of the ϕ scan peak fwhms from 4.8° to 0.89°.

(44) Cimino, A.; Marezio, M. *Phys. Chem. Solids* **1960**, *17*, 57−64.
(45) For a detailed discussion of X-ray rocking curves in thin film analysis, see: Wie, C. R. *Mater. Sci. Eng., R* **1994**, *R13*, 1−58.

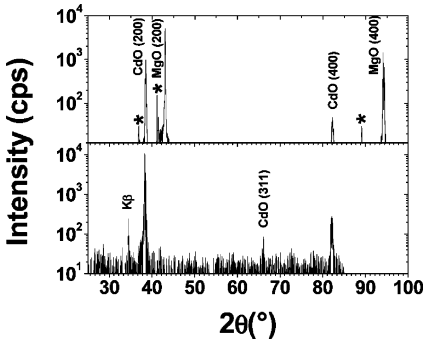

Figure 3. Representative X-ray diffraction $\theta-2\theta$ scans of CdO films grown on glass (bottom) and on MgO(100) (top) at 400 °C. XRD features marked with an asterisk (∗) denote features due to the tungsten cathode of the X-ray source.

Scanning electron microscopy (SEM) images of the present MOCVD-derived CdO films (Figure 5) reveal relatively small (<150 nm), discrete grains for each sample. Comparing the grain sizes of pairs of films on each substrate type deposited in parallel at the same temperature reveal that, in each case, the grain size of the films grown on glass is similar to or greater than that of the films grown on MgO(100).

Transmission electron microscopy (TEM) images and selected area electron diffraction (SAED) patterns of the CdO films grown at 400 °C on glass and MgO(100) are shown in Figures 6 and 7, respectively. The dark-field TEM micrographs illustrate the columnar grain growth mode of both samples. The SAED pattern of the film on glass (Figure 6B) is indicative of a polycrystalline sample with a wide distribution of crystallographic orientations, while on MgO(100) (Figure 7B) the grains retain the biaxial (in-plane and out-of-plane) texture of the substrate. It is also clear that this high degree of texture allows a more densely packed microstructure than on glass where crystallographic misalignment creates voids between grains.

Optical transmittance spectra and band gap estimates[47] for the present CdO films on glass and MgO are compared in Figures 8 and 9. The appreciable variation of the visible region transmittance is primarily a result of differing film thicknesses. When normalized to a film thickness of 500 nm, all transmittances are greater than 80% vs the blank substrate at 550 nm. Large red-shifts in the plasma edge, the reflectance due to free carriers,[48] as deposition temperature increases suggest large decreases in the film carrier concentration (see further Discussion below). Band gaps are estimated from the optical transmittance spectra, assuming a direct band gap[7] and decrease from 3.05 to 2.84 eV, and 2.97 to 2.78 eV with increasing deposition temperature (300 → 412 °C) for films on glass and MgO(100), respectively. Derived CdO band gaps are compiled in Table 3.

(46) X-ray ϕ-scans are often used for the analysis of in-plane film texture: (a) Towner, D. J.; Ni, J.; Marks, T. J.; Wessels, B. W. *J. Cryst. Growth* **2003**, *255*, 107−113. (b) Sun, Y. J.; Brandt, O.; Liu, T. Y.; Trampert, A.; Ploog, K. H.; Blasing, J.; Krost, A. *Appl. Phys. Lett.* **2002**, *81*, 4928−4930. (c) Savvides, N.; Thorley, A.; Gnanarajan, S.; Katsaros, A. *Thin Solid Films* **2001**, *388*, 177−182. (d) Babcock, J. R.; Benson, D. D.; Wang, A.; Edleman, N. L.; Belot, J. A.; Metz, M. V.; Marks, T. J. *Chem. Vap. Deposition* **2000**, *6*, 180−183. (e) Wang, A.; Belot, J. A.; Marks, T. J.; Markworth, P. R.; Chang, R. P. H.; Chudzik, M. P.; Kannewurf, C. R. *Physica C (Amsterdam)* **1999**, *320*, 154−160. (f) Kang, Y. M.; Ku, J. K.; Baik, S. *J. Appl. Phys.* **1995**, *78*, 2601−2606.
(47) Pankove, J. *Optical Processes in Semiconductors*; Dover: New York, 1976; Chapter 3, p 36.
(48) (a) Howson, R. P. *J. Phys. D: Appl. Phys.* **1970**, *3*, 863−870. (b) Rauluszkiewicz, J.; Sniadower, L. *Przegl. Elektron.* **1965**, *6*, 477−487.

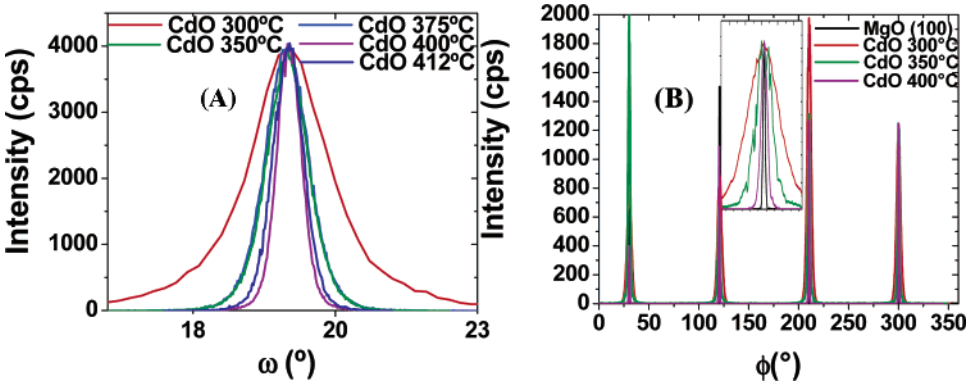

Figure 4. X-ray diffraction texture analysis of CdO films grown on MgO(100). (A) Rocking curves of the (200) reflection. (B) ϕ scans of the (111) reflections.(Inset) Expansion of the reflections at ∼300°.

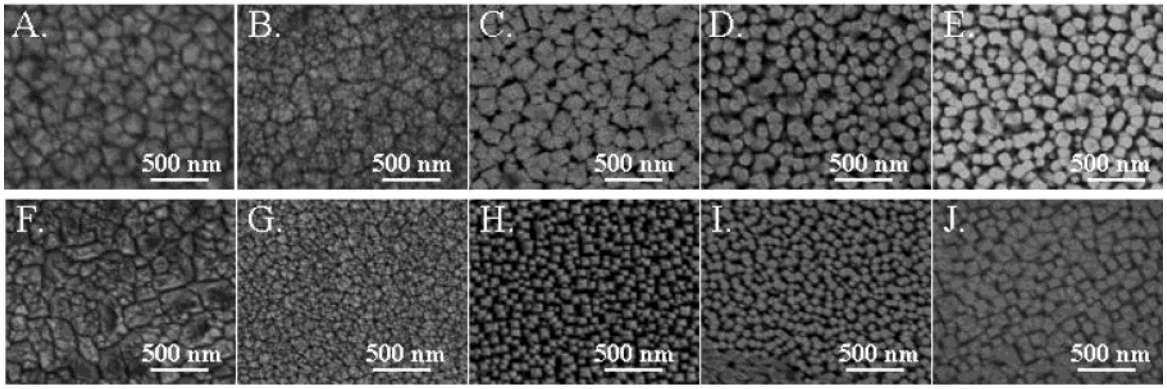

Figure 5. SEM images of CdO films grown on 1737F glass deposited at: (A) 300 °C, (B) 350 °C, (C) 375 °C, (D) 400 °C, and (E) 412 °C; on MgO(100) deposited at: (F) 300 °C, (G) 350 °C, (H) 375 °C, (I) 400 °C, (J) 412 °C.

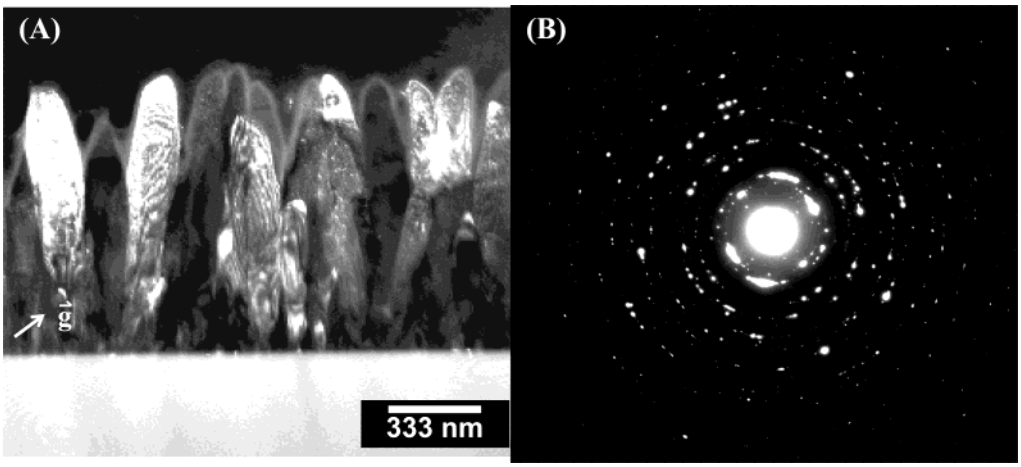

Figure 6. Cross-sectional TEM of CdO films grown on 1737F glass at 400 °C. (A) Dark-field image. (B) Selected area electron diffraction pattern.

Figures 10 and 11 compare the charge transport characteristics of the CdO films grown on glass and MgO, respectively, as determined from variable-temperature Hall effect and four-probe conductivity. All films display temperature-independent carrier concentrations, indicative of degenerate semiconductor behavior,[49] and all films are *n*-type (the majority of charge carriers are electrons). For films on glass, the mobilities and conductivities are largely independent of temperature. However, slight positive slopes are observed above temperatures of 150 K for films deposited at or below 400 °C, and a slight negative slope in the same temperature range is viewed for the film grown at 412 °C. The mobilities and conductivities of the CdO films on MgO(100) are temperature-independent at low deposition temperatures, while a negative slope becomes increasingly more noticeable at higher deposition temperatures. Room temperature values of conductivity, carrier concentration, and mobility are summarized in Table 3. The room-temperature mobilities increase with deposition temperature more rapidly than the carrier concentrations decrease, resulting in growth of the most conductive films at 412 °C.

Slow CdO Film Growth on MgO(100)**.** For this series of films, the Ar carrier gas flow rate through the Cd precursor reservoir was reduced by 50%, resulting in a significant

(49) Fan, J. C. C.; Goodenough, J. B. *J. Appl. Phys.* **1977**, *48*, 3524−3531.

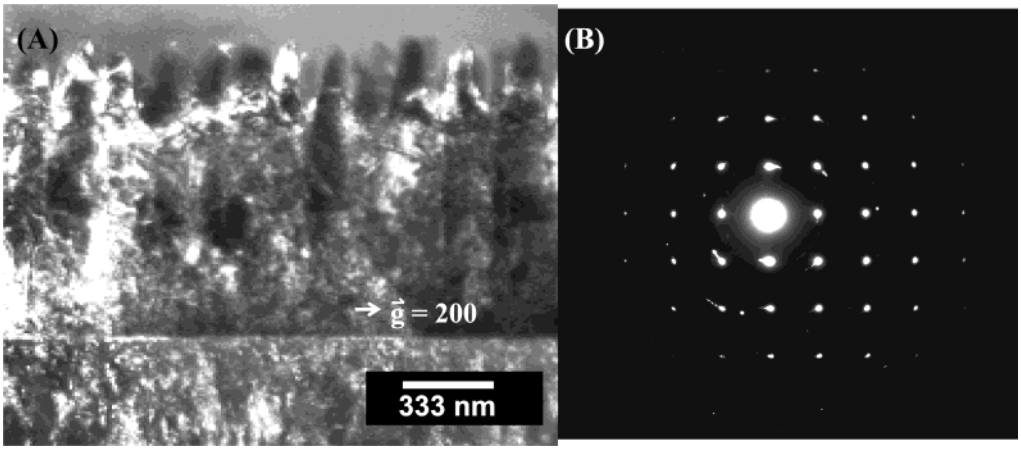

Figure 7. Cross-sectional TEM of CdO films grown on MgO(100) at 400 °C. (A) Dark-field image. (B) Selected area electron diffraction pattern.

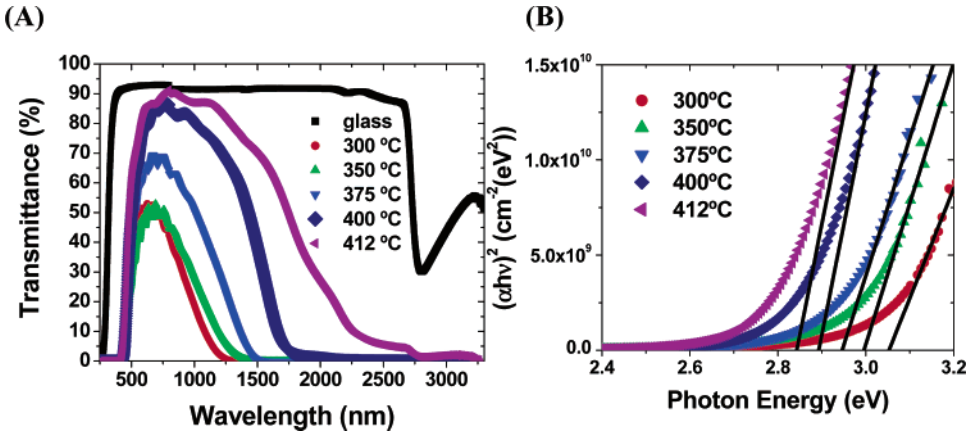

Figure 8. Optical characterization of CdO films grown on Corning 1737F glass: [black ■] at 300 °C [red ●], 350 °C [green ▲], 375 °C [blue ▼], 400 °C [black ◆], 412 °C [solid magenta triangle pointing left]. (A) Optical transmission spectra. (B) Band gap estimations.

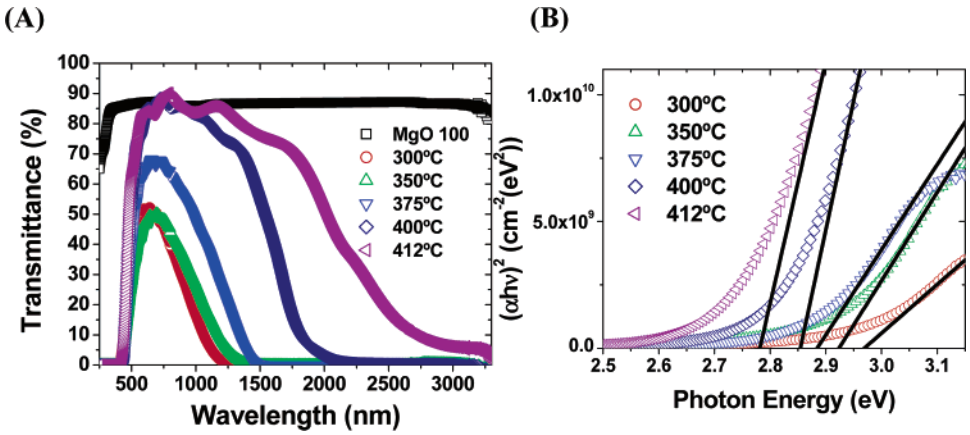

Figure 9. Optical characterization of CdO films grown on MgO(100): [□] at 300 °C [red ○], 350 °C [green △], 375 °C [blue ▽], 400 °C [black ◇], 412 °C [open magenta triangle pointing left]. (A) Optical transmission spectra. (B) Band gap estimations.

depression in growth rate. Film growth rates in this series exhibit two distinct regimes. Initially, a decrease in growth rate from 0.32 μm/h to 0.18 μm/h is observed over the increasing substrate temperature range 300−375 °C. Then at 400 °C, the growth rate increases to 0.58 μm/h and then decreases with increasing substrate temperature. As in the case of the CdO films discussed above (Figures 3 and 4), XRD confirms highly crystalline, phase-pure CdO with the cubic rock-salt crystal structure. $\theta-2\theta$ scans reveal features only from the (200) and (400) reflections of the substrate and film. A slightly greater degree of out-of-plane texture is observed by ω-scan fwhm data for the (200) reflection, which decreases from 1.0° to 0.30° as the deposition temperature is increased from 300 to 400 °C. The biaxial texture of these films was confirmed using ϕ scans of the (111) reflections, which reveal four peaks, each separated by 90° increments. A large degree of in-plane-texture with $\text{fwhm}_\phi = 0.27°$ is observed for the film grown at 400 °C.

SEM images (Figure 12) confirm the successful manipulation of CdO film microstructure by slowing the growth rate. At low deposition temperatures, film microstructure is much like that of films grown with higher precursor delivery rates. However, grains become elongated and begin to coalesce at ∼375 °C. At

Table 3. Summary of Optical and Electrical Properties of CdO Films Grown Simultaneously on MgO(100) and Corning 1737F as a Function of Deposition Temperature

deposition temp (°C)	substrate	thickness (nm)	band gap (eV)	σ_{298} (S/cm)	N_{298} (cm^{-3})	μ_{298} ($cm^2/V\cdot s$)
300	1737F	1630	3.05	760	1.24×10^{21}	3.80
350	1737F	1430	2.99	534	9.80×10^{20}	3.40
375	1737F	1240	2.95	1830	6.14×10^{20}	18.6
400	1737F	940	2.89	2860	3.82×10^{20}	46.7
412	1737F	530	2.84	4900	2.91×10^{20}	105
300	MgO(100)	1690	2.97	–	–	–
350	MgO(100)	1400	2.92	3540	1.18×10^{21}	18.7
375	MgO(100)	1410	2.88	4830	8.19×10^{20}	36.8
400	MgO(100)	780	2.85	8590	4.49×10^{20}	119
412	MgO(100)	510	2.78	7360	2.84×10^{20}	162

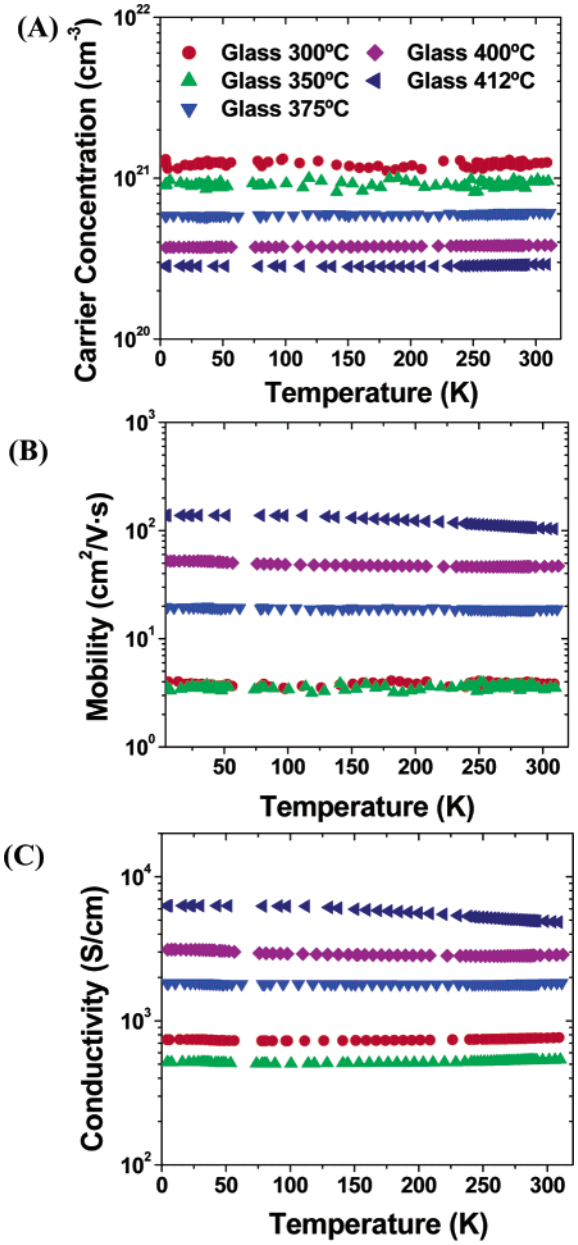

Figure 10. Variable-temperature Hall effect and four-probe charge transport measurements for CdO films grown on Corning 1737F glass at temperatures of: 300 °C [red ●], 350 °C [green ▲], 375 °C [blue ▼], 400 °C [magenta ◆], 412 °C [solid black triangle pointing left]. (A) Carrier concentration. (B) Hall mobility. (C) Conductivity.

393 °C, the film morphology is not homogeneous to the naked eye, and consists of two distinct regions. The image in Figure

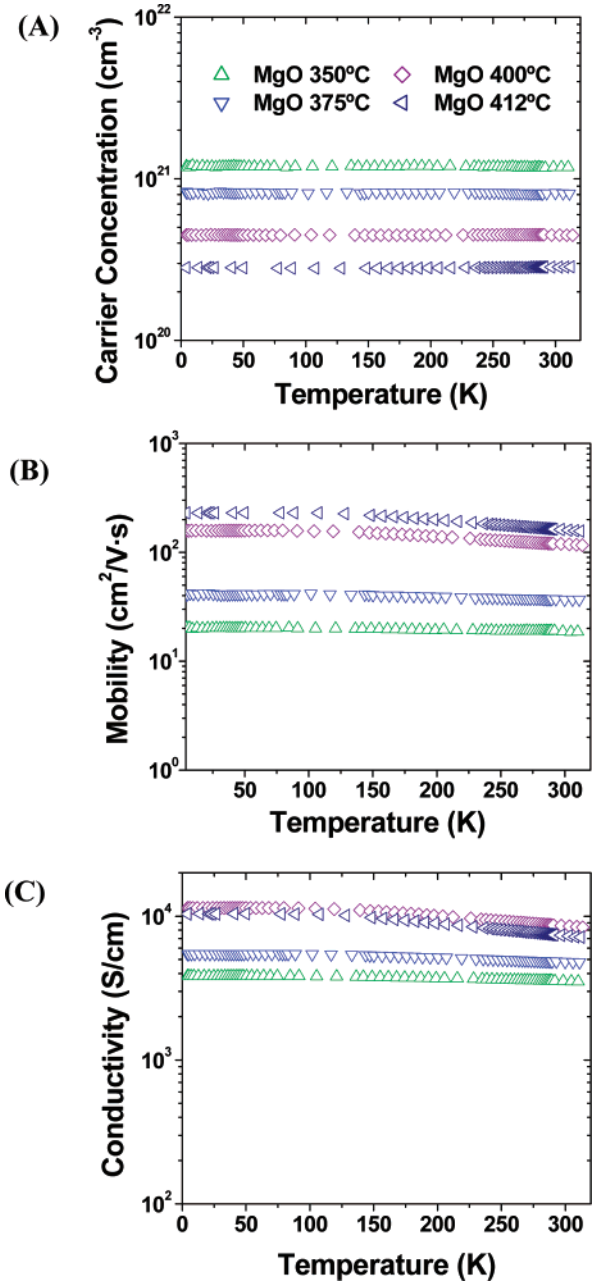

Figure 11. Variable-temperature Hall effect and four-probe charge transport measurements for CdO films grown on MgO(100) at temperatures of: 350 °C [green △], 375 °C [blue ▽], 400 °C [magenta ◇], 412 °C [open black triangle pointing left] (A) Carrier concentration (B) Hall mobility (C) Conductivity.

12D reveals the intersection of these two regions. A layer of discrete grains is clearly visible with a single grain overgrowth. At 400 °C deposition temperatures and higher, the films appear smooth and featureless by SEM. Note that this single-grain growth regime coincides with relaxation of the measured film lattice parameter to the CdO bulk value and the observed abrupt increase in growth rate. At lower deposition temperatures, the observed lattice parameters are smaller than the bulk values due to the relatively large lattice mismatch between the MgO substrate and the CdO crystal structure (10.2%) and scale approximately with film thickness. Analogous efforts to manipulate the microstructure of films on glass via slow growth achieve no significant increase in grain size.

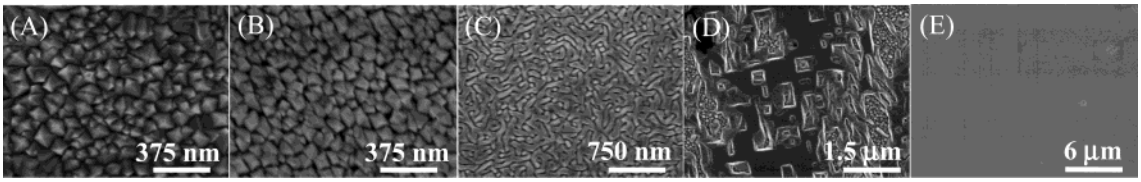

Figure 12. SEM images of CdO on MgO(100) deposited at: (A) 300, (B) 335, (C) 375, (D) 393, and (E) 412 °C under slow-growth conditions.

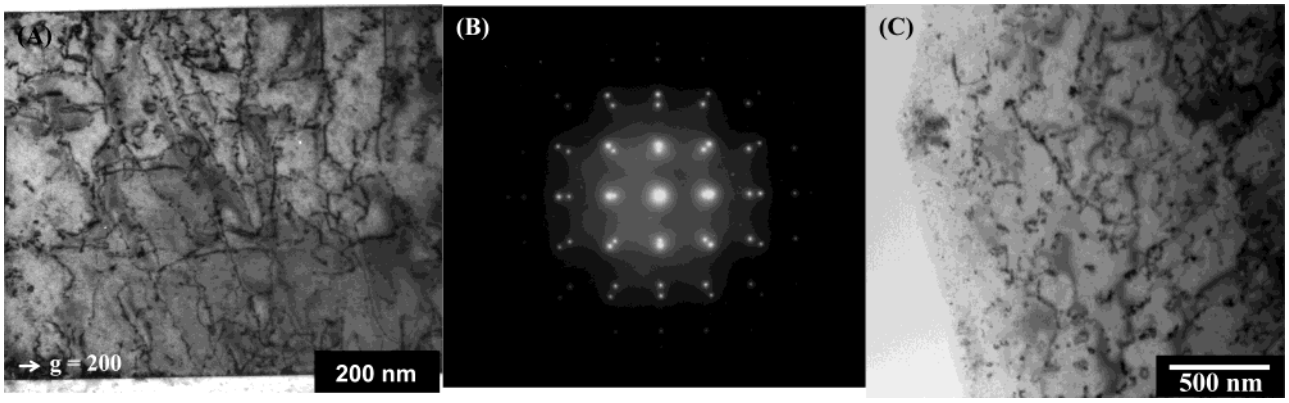

Figure 13. TEM of CdO films deposited on MgO(100) at 400 °C under slow-growth conditions. (A) Bright-field cross-sectional image. (B) Selected area electron diffraction pattern. (C) Plan-view bright-field image.

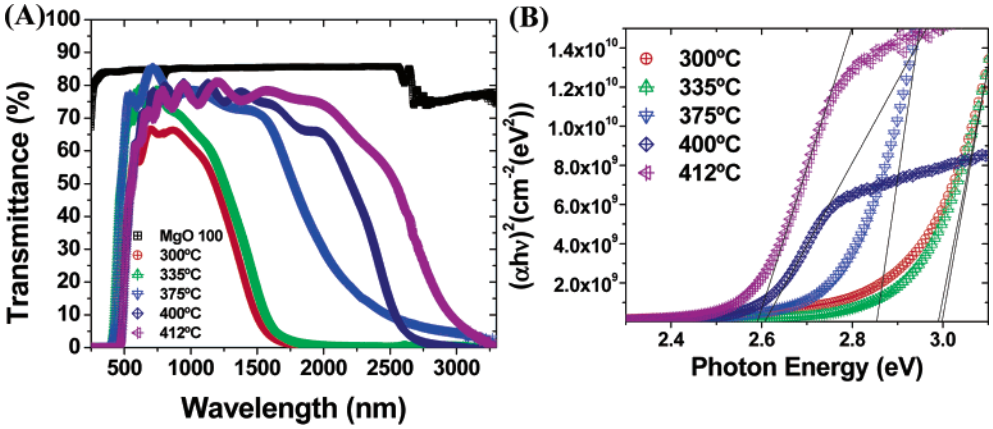

Figure 14. Optical characterization of CdO films grown on MgO(100) [⊡] at 300, 350, 375, 400, 412 °C under slow-growth conditions. (A) Optical transmission spectra. (B) Band gap estimations.

TEM micrographs and SAED patterns of the CdO film grown slowly at 400 °C are shown in Figure 13. The electron diffraction pattern along the [100] zone axis confirms the epitaxial,[50] cube-on-cube, film/substrate relationship. The cross-sectional bright-field image reveals an abrupt film/substrate interface with no evidence of a seed layer as implied by the SEM results on the 393 °C slow-growth CdO film. Threading dislocations are seen extending from the film/substrate interface to the film surface and most likely serve to reduce the lattice strain caused by the film/substrate lattice mismatch. Although transparent single-crystal substrates with closer lattice matches to CdO are available, the cost of the best candidate, single-crystal ZnO, prohibits extensive experimentation. Furthermore, use of MgF_2 substrates results in randomly oriented polycrystalline CdO films with no transfer of texture from the substrate. The plan-view bright-field image (Figure 13C) confirms the single-grain nature of the film. No grain boundaries are observed over a lateral distance on the order of 10 μm.

(50) Roy, R.; Guo, R.; Bhalla, A. S.; Cross, L. E. *J. Vac. Sci. Technol., A* **1994**, *12*, 269−273.

Table 4. Summary of Optical and Electrical Properties of CdO Films Grown on MgO(100) under Slow-Growth Conditions as a Function of Deposition Temperature

deposition temp (°C)	substrate	thickness (nm)	band gap (eV)	σ_{298} (S/cm)	N_{298} (cm^{-3})	μ_{298} (cm^2/V·s)
300	MgO(100)	630	2.99	2750	1.96×10^{21}	8.76
335	MgO(100)	590	3.00	2250	6.89×10^{20}	20.4
375	MgO(100)	350	2.85	6880	5.05×10^{20}	85.0
400	MgO(100)	1150	2.61	11000	2.23×10^{20}	307
412	MgO(100)	910	2.59	9320	2.07×10^{20}	281

Optical transmittance spectra and band gap estimates for "slow-growth" CdO films are shown in Figure 14. Again, the appreciable variation in film transmittance in the visible region is mostly an artifact of film thickness, and large shifts in the plasma edge are observed. Band gaps decrease from 2.99 to 2.59 eV with increasing deposition temperature. Derived optical parameters are compiled in Table 4.

Figure 15 summarizes the charge transport characteristics of slow-growth CdO films as determined from variable-temperature Hall and four-probe conductivity measurements. All films display temperature-independent carrier concentrations, indica-

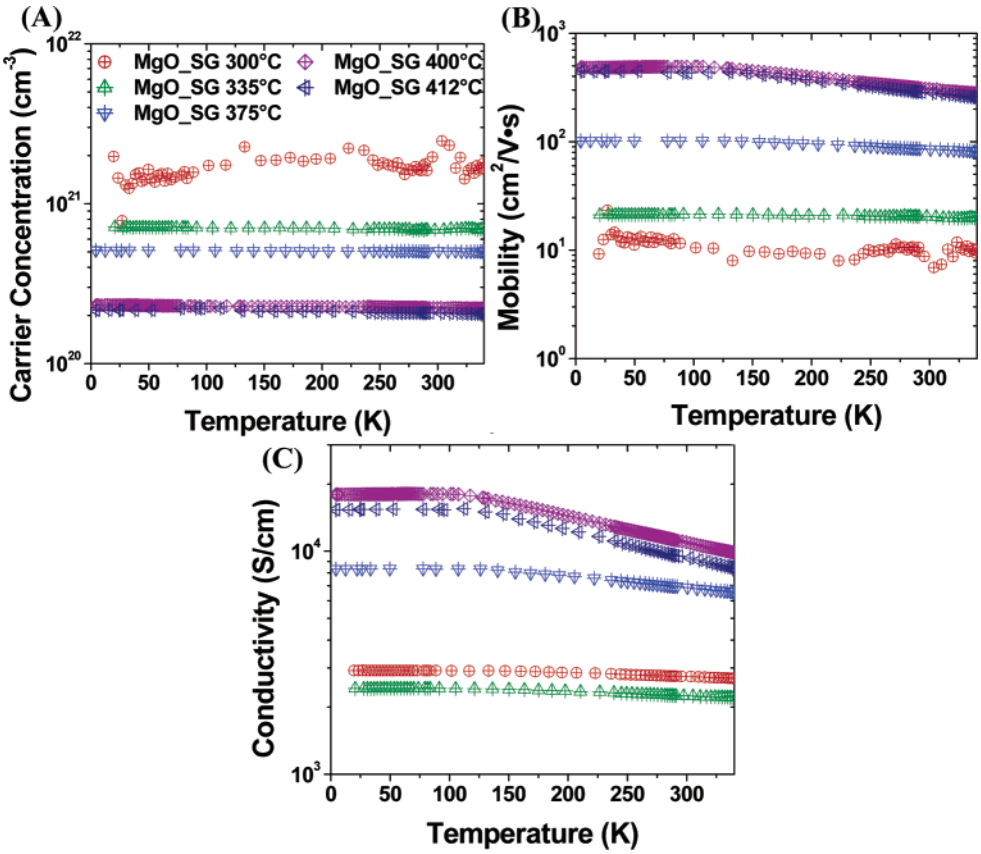

Figure 15. Variable-temperature Hall effect and four-probe charge transport measurements on CdO films grown on MgO(100) under slow-growth conditions at temperatures of: 300 °C [red circled +], 350 °C [open green triangle up symbol], 375 °C [open blue triangle down symbol], 400 °C [black tilted square with +], 412 °C [open magenta triangle pointing left with +]. (A) Carrier concentration. (B) Hall mobility. (C) Conductivity.

tive of degenerate semiconductor behavior (Figure 15A) and are n-type. Mobilities and conductivities (Figure 15B,C) are temperature-independent for low growth temperatures while a negative slope becomes increasingly more noticeable at higher growth temperatures. Room-temperature values of conductivity, carrier concentration, and mobility are summarized in Table 4. Room-temperature mobility and conductivity reach appreciable maxima at ~400 °C (307 $cm^2/V\cdot s$ and 11 000 S/cm, respectively), while carrier concentrations decrease across the series.

Optical reflectivity measurements for films deposited on MgO(100) at 400 °C are shown in Figure 16. Plasma frequency and scattering time derived from a Drude analysis are included in the figure legend. The film with small grains exhibits an ~5.7× smaller scattering time than the single-grained film, 2.43×10^{-14} vs 1.39×10^{-13} s, respectively. In principle, effective medium approximation calculations should be carried out for the small-grained film, but as a first approximation we neglect it here. Some of the smearing in the small-grain film data can be attributed to light scattering, owing to surface roughness on the order of the grain sizes. We estimate that the true scattering rate in this film could be lower by as much as a factor of 2 (or a factor of 2 larger scattering time).

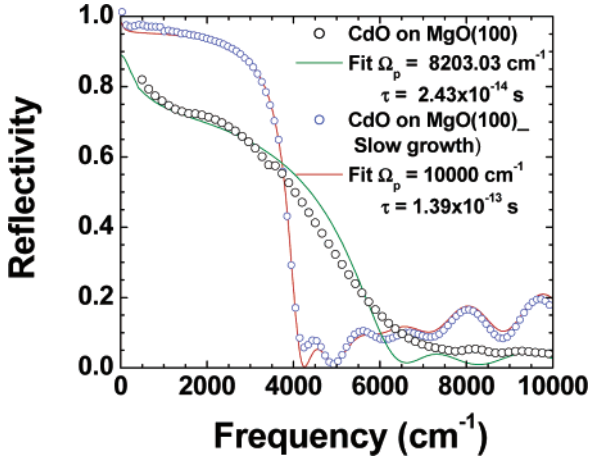

Figure 16. Optical reflectance measurements of CdO films grown at 400 °C on MgO(100) and on MgO(100) under slow-growth conditions.

Discussion

Precursors. The synthetic coordination chemistry aspect of this work was undertaken to provide efficient Cd MOCVD precursor alternatives to dimethylcadmium. An ideal MOCVD precursor should be a highly volatile, thermally stable, low-melting solid, which is air- and moisture-stable, easy to synthesize and handle, and which possesses minimal toxicity. We are not aware of a Cd precursor that fulfills all of these requirements. The present synthesis of lower-melting analogues of $Cd(hfa)_2(TMEDA)$ was achieved by varying the alkyl substituents on the chelating diamine ligand. The result of these substitutions is successful tailoring of melting points, with $Cd(hfa)_2$(diamine) complexes **2**−**4** fulfilling all of the above requirements. Of the four new precursors, complex **3** was chosen for film-growth experiments because it displays the optimum combination of low-melting point and high volatility, and is demonstrated here to be an efficient precursor for growth of high-quality CdO thin films.

Precursor Synthesis, Molecular Structures, and Properties. When seeking alternative MOCVD precursors to metal alkyls, simple β-diketonates are often the first compounds to be explored because of their broad chemical versatility, ready accessibility, and ability to saturate the coordination spheres of many metal centers. However, as illustrated by the polymeric crystal structure of $[Cd(acac)_2]_n$ shown below,[51] metal coordination sphere saturation is sometimes not complete in simple homoleptic metal β-diketonate complexes.

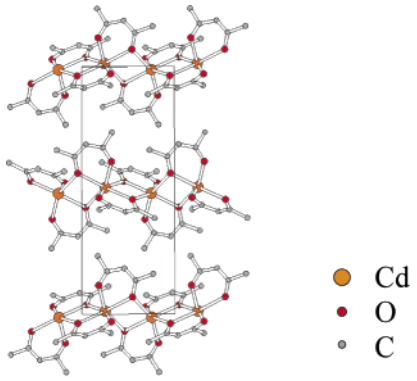

$[Cd(acac)_2]_n$

Oligomerization results in greatly increased molecular weights and lattice cohesive energies and thus seriously diminishes volatility. The use of an additional neutrally charged ancillary ligand is one strategy for achieving coordinative saturation and has proven effective for Ba^{2+} precursors.[32,35,52−54] Our approach for Cd^{2+} was to combine a volatility- and Lewis acidity-enhancing fluorinated β-diketonate ligand, hexafluoroacetoacetonate (hfa), with a bidentate nitrogenous ancillary donor ligand to maximize thermal stability while saturating the metal coordination sphere, hence ensuring thermal stability and volatility. The crystal structures of complexes **1** and **4** (Figure 1) show that this approach is successful in saturating the metal coordination sphere, as desired. Furthermore, it is well-established that β-diketonate ligand fluorination ehances the binding strength of neutral ancillary ligands by withdrawing electron density from the metal center, thus increasing Lewis acidity.[52,55] Following the same argument, diamine donors should enhance thermal stability more than analogous glyme adducts due to the greater Lewis basicity of amines vs ethers.[53] Both concepts are critical to the robust thermal stability of complex **3.** This is readily seen by comparing the significant thermal decomposition of previously reported $Cd(dpm)_2$-(TMEDA)[31] and $Cd(hfa)_2$(monoglyme)[38] complexes in TGA experiments, versus the present data (Figure 2).

The synthesis of complexes **1**−**4** is readily accomplished in a single aqueous medium step under ambient conditions from commercial materials. Facile purification by sublimation allows large batches (>70 g) to be produced and purified in less than 1 day. These complexes are crystalline solids at room temperature, meaning that weighing and loading into precursor reservoirs is straightforward, in contrast to compounds which are waxy solids or viscous liquids. The tailoring of precursor melting point is one of the most important aspects of precursor development. While precursors which are crystalline solids at room temperature are desirable for ease of handling, if they remain solids at operating temperatures, poor film compositional control often results. The reason is that solid precursors undergo sintering at elevated temperatures, giving rise to time-dependent surface area and hence to time-dependent transport rates. In coordination complex systems such as the present in which precursor transport rate, or film growth rate, is largely diffusion-limited,[32] solid sources must often be used with a temperature ramp[56] or be periodically removed from the reactor system and reground (requiring a halt in the growth process) to maintain temporally constant volatilization rates. However, if a precursor is a liquid at reactor-operating temperatures, constant surface area is maintained, assuming the reservoir is of appropriate shape and volume. A strategy for lowering the melting points of these types of complexes is to reduce molecular symmetry by proper modification of ligand alkyl subsituents, which disrupt crystal packing.[57] If these modifications are effected at the ligand periphery, there is often little influence on precursor thermal stability properties.[34−36] In this work, tetramethylethylenediamine was replaced with the two structural isomers of diethylethylenediamine and diethyldimethylethylenediamine. Complexes **2**−**4** have significantly lower melting points than $Cd(hfa)_2$(TMEDA) and are liquids at temperatures which provide sufficient volatilization rates for efficient operation pressure (1−5 Torr) MOCVD reactor.

Trends in precursor melting point and volatility cannot be rigorously correlated due to the limited database and many variables involved; however, they provide useful qualitative insight into effects substitutions can have. Excluding the behavior of complex **2**, which will be discussed later, all trends are understandable. Complexes containing diamines with lower symmetry and larger, unsymmetrical alkyl substituents have lower melting points than does the TMEDA complex. Similarly, the *N*,*N*-DE-*N*′,*N*′-DMEDA adduct (**3**) has a lower melting point than the complex with the higher symmetry structural isomer, *N*,*N*′-DE-*N*′,*N*′-DMEDA (**4**) (Chart 1). The anomalous volatility behavior and melting point of precursor **1** can be explained by the presence of the NH_2 functionality. The low NH_2 steric bulk renders this hydrogen-bond donor accessible to neighboring molecules. Examination of the crystal structure packing diagram (shown in Supporting Information) of complex **1** reveals layers of hydrogen-bonded dimer units in which the NH_2 functionality serves as a hydrogen-bond donor to F and O atoms of an hfa ligand of the adjacent molecule. Hydrogen-bond distances are summarized in Table 5 and are consistent with weak hydrogen bonds.[58]

CdO Film Growth and Characterization. CdO film growth by MOCVD was carried out to demonstrate the utility of the

(51) Maslen, E. N.; Greaney, T. M.; Raston, C. L.; White, A. H. *J. Chem. Soc., Dalton Trans.* **1975**, 400−402.
(52) Gardiner, R.; Brown, D. W.; Kirlin, P. S.; Rheingold, A. L. *Chem. Mater.* **1991**, *3*, 1053−1059.
(53) Gardiner, R. A.; Gordon, D. C.; Stauf, G. T.; Vaartstra, B. A.; Ostrander, R. L.; Rheingold, A. L. *Chem. Mater.* **1994**, *6*, 1967−1970.
(54) Otway, D. J.; Rees, W. S., Jr. *Coord. Chem. Rev.* **2000**, *210*, 279−328.
(55) (a) Watson, I. M.; Atwood, M. P.; Haq, S. *Supercond. Sci. Technol.* **1994**, *7*, 672−680. (b) Malandrino, G.; Richeson, D. S.; Marks, T. J.; DeGroot, D. C.; Schindler, J. L.; Kannewurf, C. R. *Appl. Phys. Lett.* **1991**, *58*, 182−184. (c) Timmer, K.; Spee, K. I. M. A.; Mackor, A.; Meinema, H. A.; Spek, A. L.; Van der Sluis, P. *Inorg. Chim. Acta* **1991**, *190*, 109−117.
(56) Liang, S.; Chern, C. S.; Shi, Z. Q.; Lu, P.; Lu, Y.; Kear, B. H. *J. Cryst. Growth* **1995**, *151*, 359−364.
(57) Brown, R. J. C. *J. Chem. Educ.* **2000**, *77*, 724−731.
(58) Hamilton, W. C.; Ibers, J. A. *Hydrogen Bonding in Solids, Methods of Molecular Structure Determination (Frontiers in Chemistry)*; W. A. Benjamin: New York, 1968.

Chart 1

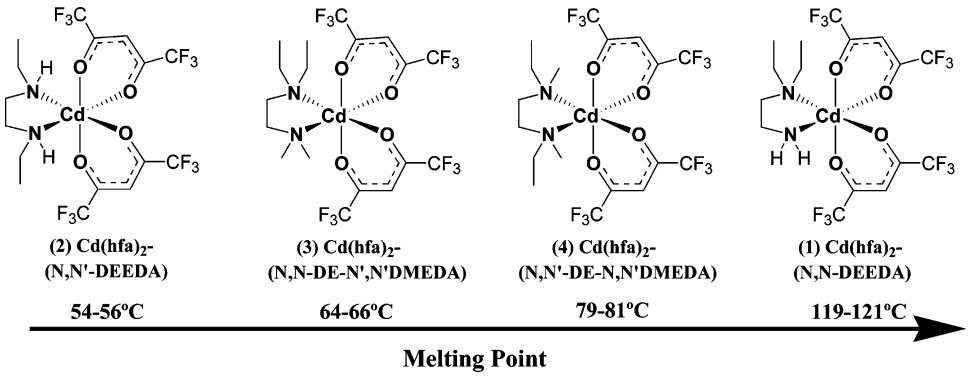

Table 5. Intermolecular Hydrogen-Bond Distances (Å) in Complex **1**

H-bond	DH	HA	DA
N2−H2D···O4	0.90(5)	2.55(5)	3.159(5)
N2−H2D···F10	0.90(5)	2.59(6)	3.467(5)
N2−H2C···O2	0.87(6)	2.31(6)	3.152(5)
N2−H2C···F6	0.87(6)	2.64(6)	2.275(5)

Cd precursors synthesized in this study as well as to attempt to elucidate the effects of epitaxy and microstructure on TCO optical and charge transport properties. A better fundamental understanding of how to tailor the optoelectronic properties of oxide materials is of broad interest, and the ability to better tailor degenerate semiconductor carrier mobility is of particular interest to the TCO community.

One obvious concern arising from the use of fluorinated ligands in the precursor architecture is the possibility of fluoride phase formation/contamination/doping (F^- substitution for O^{2-}) during the growth process. A well-known method for minimizing F^- incorporation is including H_2O in the oxidant stream as was done here.[59] For all CdO films grown in this work, F^- concentrations were found to be below the detection limits of EDS measurements (∼1.5%). In addition, quantitative SIMS analysis of CdO films deposited using $Cd(hfa)_2$(TMEDA) under nearly identical growth conditions (365 °C, 300 sccm H_2O saturated O_2, 4 Torr working pressure) revealed F^- concentrations of $\sim 1 \times 10^{20}$ cm^{-3} or 0.26 atomic %. At this level, it is unlikely that F^- would significantly effect film mircrostructural characteristics. There is also no reason to believe any difference in F^- concentration would be observed in films deposited simultaneously on different substrate types. Therefore, it is physically reasonable, when comparing films grown in the same precursor stream at the same temperature, that differences observed in charge transport behavior are not due to differences in adventitious F^- contamination. Furthermore, even assuming the unlikely extreme of 100% doping efficiency in the films having the lowest carrier concentrations, less than half of the observed carriers could derive from F^- doping. In a practical sense, any such fortuitous doping provides an efficient method of maintaining useful carrier concentrations along with extremely high mobilities, something not previously accomplished in MOCVD-derived CdO films grown using $CdMe_2$.[3,8,12,13,16]

CdO Film Microstructure/Morphology Constraints on Charge Transport. As can be seen in Figure 17, each series of CdO films grown in this study exhibits an increase in carrier mobility that correlates with increasing deposition temperature. This correlation between deposition temperature and mobility was previously observed in MOCVD-derived CdO films on glass[3,8,12,13] and was attributed primarily to improved intragrain quality and crystallinity. However, in the cited work, increasing grain size and decreased carrier concentrations were also observed, and all have the potential to effect carrier mobility in the following ways: (1) It is well-known that potential energy barriers at grain boundaries can limit carrier mobilities in polycrystalline semiconductors having small grains.[14,17,18,60] (2) Carriers are generated in conjunction with ionized defects, which then serve as scattering centers and reduce mobility. Furthermore, in materials such as CdO that have nonparabolic conduction bands[3,7,10,61] effective carrier mass and therefore mobility should to some degree be dependent on carrier concentration.[17] (3) Enhanced film crystallinity, resulting from increased deposition temperatures or from epitaxy, has also been associated with increased carrier mobility.[8,13,22,23,26,62] Given that three parameters which may have effects on mobility are varying simultaneously, it has not previously been possible to rigorously differentiate among the relative contributions of these effects. This issue in part motivated the systematic experimental design in the present work where great care is taken to attempt to isolate the individual effects.

The temperature dependence of mobility in degenerate semiconductors/transparent conductors has been discussed previously.[18,19,23] An expression for mobility limited only by lattice vibration scattering (LVS) is given in eq 2,[17,63] revealing the primary temperature dependence as $\mu_L \propto T^{-1}$.

$$\mu_L = 9.67 \times 10^3 \left(\frac{C_l}{10^{12}\ \mathrm{dyn\ cm^{-1}}}\right)(m^*)^{-5/2} \cdot \left(\frac{300k}{T}\right)\left(\frac{eV}{E_d}\right) \times \left(\frac{10^{19} cm^{-3}}{n}\right)^{1/3} \quad (2)$$

Here C_l is the longitudinal sound velocity, and E_d is the deformation potential. Mobilities which are dominated by neutral impurities (μ_N) or ionized impurities (μ_I) have been described

(59) (a) Pinkas, J.; Huffman, J. C.; Baxter, D. V.; Chisholm, M. H.; Caulton, K. G. *Chem. Mater*. **1995**, *7*, 1589−1596. (b) Kaloyeros, A. E.; Zheng, B.; Lou, I.; Lau, J.; Hellgeth, J. W. *Thin Solid Films* **1995**, *262*, 20−30. (c) Lecohier, B.; Calpini, B.; Philippoz, J. M.; Van den Bergh, H. *J. Appl. Phys.* **1992**, *72*, 2022−2026.

(60) Seto, J. Y. W. *J. Appl. Phys.* **1975**, *46*, 5247−5254.

(61) (a) Koffyberg, F. P. *Can. J. Phys.* **1971**, *49*, 435−440. (b) Koffyberg, F. P. *J. Solid State Chem.* **1970**, *2*, 176−181.

(62) (a) Taga, N.; Shigesato, Y.; Kamei, M. *J. Vac. Sci. Technol., A* **2000**, *18*, 1663−1667. (b) Ohta, H.; Orita, M.; Hirano, M.; Tanji, H.; Kawazoe, H.; Hosono, H. *Appl. Phys. Lett.* **2000**, *76*, 2740−2742.

(63) Bardeen, J.; Shockley, W. *Phys. Rev.* **1950**, *80*, 72−80.

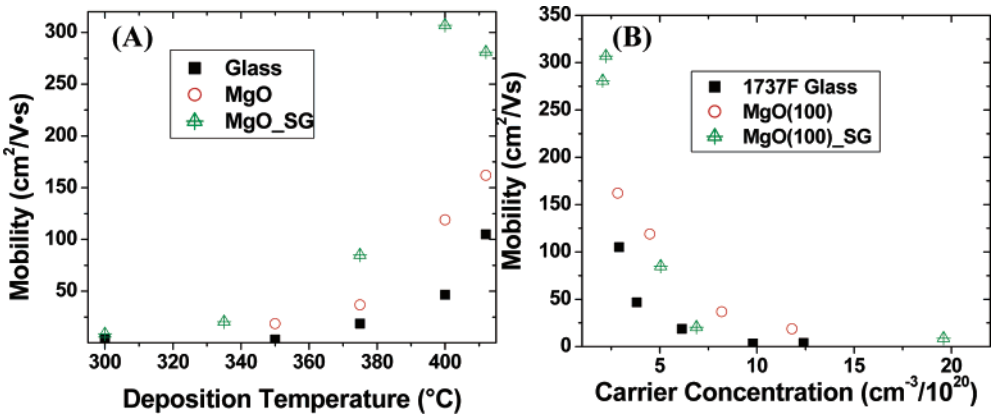

Figure 17. Room-temperature Hall effect mobilities as a function of: (A) film growth temperature and (B) carrier concentration for films on 1737F glass [black squares], MgO(100) [red circles], and MgO(100) under slow-growth conditions [green triangle symbols].

previously and within these models exhibit essentially temperature-independent behavior (eqs 3,4),[23,64]

$$\mu_N = (m^* e^3)/(20\epsilon_0\epsilon_r\hbar^3 n_N) \quad (3)$$

$$\mu_I = [24\pi^3(\epsilon_0\epsilon_r)^2\hbar^3 n]/[e^3 m^{*2} g(x) Z^2 n_I] \quad (4)$$

where the screening function $g(x)$ is given by eqs 5 and 6,

$$g(x) = \ln(1 + 4/x) - (1 + x/4)^{-1} \quad (5)$$

and where

$$x = \frac{4e^2 m^*}{4\pi\epsilon_0\epsilon_e\hbar^2(3\pi^5)^{1/3} n^{1/3}} \quad (6)$$

Here, ϵ_r is the low-frequency relative permittivity, n_N the concentration of neutral scattering centers, Z and n_I the charge and concentration of ionized scattering centers, respectively, and m^* is the effective mass, all of which are assumed to be temperature-independent.

The temperature dependence of mobility limited by grain boundary scattering is not as straightforward because of two distinct mechanisms for charge transport across grain boundaries. Application of Fermi−Dirac statistics to the Petritz model[65] gives eq 7,[18,66]

$$\mu_g = BT^{-1}\exp\left(-\frac{eV_a}{kT}\right) \quad (7)$$

where B is a constant and V_a represents an activation energy related to the barrier V_b by the expression $V_a = V_b - (E_F - E_c)$. E_F and E_c are the Fermi energy and the lowest conduction band energy, respectively. However, thermionic emission should only dominate transport across potential barriers at low carrier concentrations and in the degenerate regime, temperature-independent tunneling currents may make the dominant contribution.[18,67]

Figure 18 presents variable-temperature Hall effect carrier mobility data for the present CdO films grown at 400 °C on glass, MgO(100) with discrete grains, and MgO(100) with coalesced grains. For a degenerate semiconductor, the mobility of which is governed solely by ionized impurity scattering, no temperature dependence should be observed. Although all three CdO film samples have essentially temperature-independent mobilities below 100 K, the observed temperature dependence above 200 K increases from $T^{-0.06}$ to $T^{-0.64}$ along the series glass → MgO(100) with discrete grains → MgO(100) with coalesced grains. The strong T^{-x} dependence for the samples deposited on MgO(100) argues for the importance of LVS.[17,18] The relative magnitudes of the temperature dependencies indicate that another temperature-independent scattering mechanism has a significant influence in limiting the mobility of the CdO films on glass and, to a lesser extent, for the films on MgO(100).

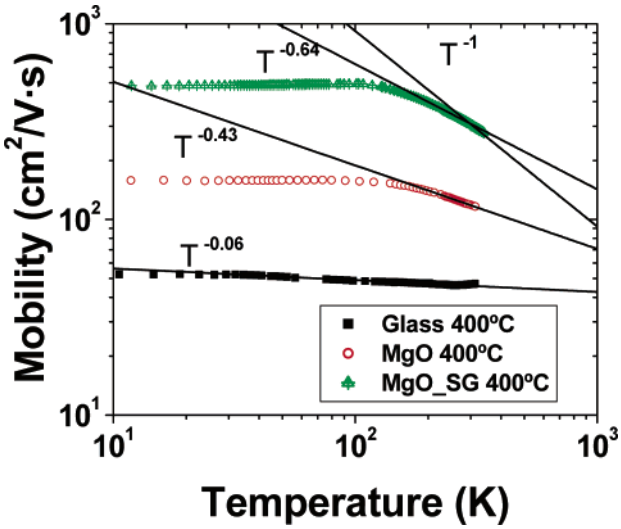

Figure 18. Variable-temperature Hall effect mobility measurements on CdO films grown at 400 °C on 1737F glass [black squares], MgO(100) [red circles], and MgO(100) under slow-growth conditions [green triangle symbols]. Linear regressions are shown (data fit between 200 and 300 K) along with the theoretical temperature dependence for mobility limited primarily by lattice vibration scattering ($\mu \propto T^{-1}$).

Glass vs MgO(100) as Substrates. A significant increase in Hall effect carrier mobility is observed for all CdO films grown on single-crystal MgO(100) compared to those grown in parallel on glass. Considering that the films on MgO(100) have, in general, higher carrier concentrations, and similar or smaller grain sizes, it seems unlikely that the mobility differences are solely due to changes in ionized impurity scattering, effective

(64) (a) Dingle, R. B. *Philos. Mag.* **1955**, *46*, 831−840. (b) Erginsoy, C. *Phys. Rev.* **1950**, *79*, 1013−1014. (c) Frank, G.; Koestlin, H. *Appl. Phys. A* **1982**, *A27*, 197−206.
(65) Petritz, R. L. *Phys. Rev.* **1956**, *104*, 1508−1516.
(66) Bruneaux, J.; Cachet, H.; Froment, M.; Messad, A. *Thin Solid Films* **1991**, *197*, 129−142.
(67) Crowell, C. R.; Rideout, V. L. *Appl. Phys. Lett.* **1969**, *14*, 85−88.

mass differences, or GBS. The only remaining major scattering mechanism which could cause this effect is NIS. Increased semiconductor mobilities have previously been attributed to a reduction in NIS caused by improved crystallinity in several cases.[8,13,22,23,26,62] The increased mobilities observed in the present study most likely have the same origin—films grown on single-crystal substrates having enhanced epitaxy-induced crystalline order. This is especially important in CdO films owing to their significant volatility, which limits the maximum deposition temperature that might otherwise be useful in improving film crystallinity. Under the present conditions, film growth attempted above 425 °C was unsuccessful, with the film growth primarily taking place on the reactor walls, and little remaining on the substrate. Another possible contribution to the increased mobility of the biaxially textured CdO films may be better intergrain contact. The highly ordered alignment of the columnar grains on MgO substrates allows a more dense and continuous film microstructure. The voids formed by the misaligned columnar grains on glass may serve as highly resistive transport pathways limiting charge mobility.

Slow Film Growth on MgO(100). While no obvious change in CdO film microstructure is observed at low deposition temperatures, reduction in precursor delivery rate induces grain coalescence beginning between growth temperatures of 350 and 375 °C and leading eventually to essentially single-grained films at or above 400 °C. These films have similar degrees of texture and 25−50% lower carrier concentrations than the first series of films on MgO(100). Since increases in mobility are not observed with similar film microstructures, but only when grain coalescence begins, this would strongly suggest that grain boundary scattering is playing a large role in limiting the mobility of these films, in agreement with the results of Yan et al. on Sn-doped pulsed laser deposition (PLD)-derived CdO films.[14]

Optical reflectivity measurements were carried out to further assess the role of GBS. Detailed analysis of the plasma edge, the reflectance within a free electron gas model, can yield information regarding charge transport properties that is complementary to Hall measurements. Hall measurements are acquired across macroscopic (∼0.5 cm)-length scales and thus can potentially be affected by GBS, if significant. In contrast, optical measurements are much less sensitive to grain boundaries as long as carrier mean-free-paths are much smaller than grain sizes. Scattering rates measured by optical spectroscopy are thus closer to bulk values. Approximate analysis allows independent determination of scattering times for the films, and data are shown in Figure 16. If the higher mobility in the single-grained CdO film in fact arises principally from reduction in GBS, then the film should have approximately the same optical scattering time as the analogous film with small grains. However, the reflectivity data clearly indicate that the scattering time of the slow-growth film is significantly larger. Therefore, it can be concluded that GBS is not a dominant process, even in high-quality epitaxial CdO films with modest carrier concentrations and small grain sizes, 2×10^{20} cm^{-3} and ∼100 nm, respectively. This conclusion is in agreement with recent results suggesting that GBS should be insignificant in TCO films based on alternative, carrier mean-free-path arguments.[17,18,21,23,24] According to Zhang and Ma,[18] a TCO with a useful conductivity will be degenerate with a high carrier concentration, limiting the carrier mean-free-path to a value much smaller than the grain size of typical films. The formulation for carrier mean-free-path is given in eq 8.[17,18]

$$l = \left(\frac{h}{2e}\right)\left(\frac{3n}{\pi}\right)^{1/3}\mu \tag{8}$$

Utilizing this relationship, the film deposited at 400 °C on MgO(100) with discrete grains has an estimated mean-free-path of <18 nm, and therefore, the impact of GBS should be minimal. The origin of the increased mobility in the single-grained film is then best explained by differences in carrier concentration. Examination of Figure 17B reveals that all samples exhibit rapid increases in mobility as the carrier concentration drops below 4×10^{20} cm^{-3}, in agreement with the dependence of mobility on carrier concentration expected in an IIS model.[17,68] Extrapolation of the curves for the second series of film samples indicates that the greater mobilities for the single-grained film are likely a result of the 50% reduction in carrier concentration.

The highest conductivity and mobility in this study (σ = 11 000 S/cm, μ = 307 cm^2/V·s) compare favorably with the highest ever reported for CdO films. The highest mobility ever reported for a CdO-based film is 609 cm^2/V·s by Yan et al.[14] in lightly Sn-doped epitaxial samples grown by PLD. Without extrinsic doping, the same growth conditions resulted in CdO films with modest mobilities of ∼120 cm^2/V·s. In addition, although PLD is an excellent growth technique for laboratory-scale materials discovery/investigation, it requires elaborate apparatus and cannot be readily scaled up for production purposes. Other noteworthy CdO growth examples are the MOCVD-derived film samples reported by Barnes et al.[8] using $CdMe_2$ and $CBrF_3$ as the precursors. Films grown on glass at 450 °C exhibit impressive mobilities (262 cm^2/V·s). However, the growth conditions yielded films with relatively low carrier concentrations, leading to a modest conductivity of ∼1600 S/cm. In addition, the use of highly toxic precursors such as $CdMe_2$ is undesirable. To our knowledge, the highest conductivity previously reported for a CdO film without extrinsic dopants is ∼5000 S/cm in activated reactive evaporation-derived samples.[69]

The use of epitaxy and precursor-limited film growth kinetics have led to very high mobility CdO films. The increased mobility observed at higher deposition temperatures is accompanied by a decrease in band gap. In view of the red-shifting plasma edge and decreasing carrier concentrations observed in the Hall effect measurements, this decrease in band gap can be readily ascribed to a Burstein−Moss shift.[7,48] While the products of this work are very high-quality films from a charge transport point of view, the band gap is somewhat smaller than is desired for many optical applications. However, having attained extremely high-quality phase-pure CdO films, doping may provide the needed increases in band gap. For example, we have previously demonstrated in $Cd_{1-x}In_xO$ films[7] that doping can greatly increase the band gap through a Burstein−Moss shift. It is reasonable to expect that similar doping can improve film optical properties, without dramatically compromising mobility, to further improve the overall performance of CdO-based TCO films. These efforts are currently underway.

(68) Johnson, V. A.; Lark-Horovitz, K. *Phys. Rev.* **1947**, *71*, 374−375.
(69) Phatak, G.; Lal, R. *Thin Solid Films* **1994**, *245*, 17−26.

Summary and Conclusions

Four new, highly volatile, temperature- and air-stable cadmium coordination complexes have been synthesized, characterized, and evaluated as potential MOCVD precursors. Complexes **2**−**4** are liquids at CVD growth reactor-operating temperatures, and Cd(hfa)$_2$(*N*,*N*-DE-*N*′,*N*′-DEEDA) has been demonstrated to be useful in the growth of highly conductive and transparent CdO thin films by MOCVD. Reduced-pressure TGA demonstrates the high thermal stability of all four precursors. These low-melting precursors will allow careful control of composition and growth rates in more complex cadmium-containing oxide systems, owing to the constant surface area of a liquid precursor and the elimination of sintering effects detrimental to reproducible growth with solid precursors. The CdO films grown by utilizing precursor **3** have conductivities and mobilities as high as 11 000 S/cm and 307 cm^2/V•s, respectively, the highest yet reported for undoped CdO films. A reduction in NIS and/or a more densely packed microstructure of biaxially textured films grown on MgO(100) are proposed on the basis of optical reflectivity and variable-temperature Hall and conductivity measurements to be responsible for enhanced mobilities vs films grown on glass. Although single-grained films grown on MgO(100) exhibit greater mobilities than analogues with discrete ∼100 nm grains and similar texture, this effect is attributed, on the basis of charge transport and Hall effect measurements as well as optical reflectivity analysis, to differences in carrier concentration rather than to a reduction in GBS. Epitaxial growth of CdO films as demonstrated here provides an approach to extremely high performance thin-film TCO materials for high-end applications utilizing an efficient and scalable deposition technique.

Acknowledgment. We thank the NSF MRSEC Program through the Northwestern Materials Research Center (DMR-0076097), NSF (CHE-0201767), and the DOE through the National Renewable Energy Laboratory (Subcontract n.AAD-9-18668-05) for support of this research. We thank Dr. T. Jensen for assistance with the VTNMR data collection and Professor T. O. Mason for helpful discussions.

Supporting Information Available: Detailed crystallographic information and VT-NMR for selected precursor complexes. This material is available free of charge via the Internet at http://pubs.acs.org.

JA039232Z